Sessile droplets on a curved substrate: effects of line tension

2007 J. Phys. A: Math. Theor. 40 19

(http://iopscience.iop.org/1751-8121/40/1/002)

INSTITUTE OF PHYSICS PUBLISHING JOURNAL OF PHYSICS A: MATHEMATICAL AND THEORETICAL

J. Phys. A: Math. Theor. **40** (2007) 19–46 doi:10.1088/1751-8113/40/1/002

Sessile droplets on a curved substrate: effects of line tension

Luca Guzzardi[1] **and Riccardo Rosso**[2]

[1] Dipartimento di Matematica, Università della Calabria, Via Ponte Bucci-Cubo 30A, Arcavacata di Rende, 87036 Cosenza, Italy
[2] Dipartimento di Matematica and CNISM, Università di Pavia, Via Ferrata 1, 27100 Pavia, Italy

E-mail: loki_delgado@hotmail.com and riccardo.rosso@unipv.it

Received 22 June 2006, in final form 17 October 2006
Published 6 December 2006
Online at stacks.iop.org/JPhysA/40/19

Abstract
The equilibrium and stability of a sessile droplet laid on a spherical substrate in the presence of line tension are studied within a continuum approach. The destabilizing role played by the substrate's curvature is analysed in detail for both positive and negative line tensions. In the former case, several bifurcation diagrams exist which show, among other things, that stable equilibria can fail to exist when the droplet size, the substrate size and the ratio between the line and the surface tension are comparable to one another. When line tension is negative, the substrate's curvature enhances the destabilization of sessile droplets.

PACS number: 68.08.Bc

1. Introduction

Prompted also by applications in colloid science [1], the equilibrium and stability of sessile droplets laid on curved substrates have received much attention in recent years. A colloidal particle of, say, spherical shape in an emulsion is more likely to be wetted by the liquid phase that is more affine to it, the less affine liquid becoming the *dispersed* phase. Traditionally, emulsions are divided into *direct* (oil-in-water, o/w) or *inverse* (water-in-oil, w/o) emulsions, according to whether the dispersed phase is oil or water. The remaining liquid phase is called the *continuous phase*. Affinity between solid particles and the phases of an emulsion can be measured by the contact angle between the particles and the water–oil interface. When this angle, measured through the water phase, is slightly less than $\pi/2$, the particle remains at the water–oil interface, and promotes stable direct emulsions, while it promotes inverse emulsions when the contact angle slightly exceeds $\pi/2$. No stabilization occurs when the contact angle departs too much from $\pi/2$ since in that case the particle prefers to stay within the bulk of a liquid phase, aqueous or oily. Besides its wettability, the shape and the size of the particle

are among the parameters that determine which phase of the emulsion is the dispersed one. Different mechanisms exist by which solid particles stabilize emulsions [2]. To our scopes, the most interesting is that requiring adsorption of the particles at the water–oil interface followed by the formation of a film that surrounds the dispersed droplets and that hampers their coalescence. This mechanism was studied by Levine and Bowen [3, 4], who focussed on the capillary interactions between spherical particles adsorbed at a water–oil interface and obtained the free-energy change that a solid particle undergoes when it is adsorbed by a droplet. Their work has been recently extended to incorporate the effects of line tension on the adsorption free energy of a single particle [5].

In a continuum approach, line tension is viewed as the excess free energy residing on a contact line where three phases coexist. To appreciate its effects, either the droplet or the substrate should be in the submicron regime. It has been conjectured (see section 5.2 of [1]) that line tension can either stabilize an emulsion or not, depending on its sign. In fact, while a negative line tension seems to favour adsorption of solid particles, a positive line tension penalizes the three-phase contact line and so prevents adsorption of solid particles.

The sign of line tension is a debated issue in wetting science. In a phenomenological model where the line tension is a constant times the length of the contact line, it has been proved that negative line tensions would make the free-energy functional unbounded from below, so that no stable equilibria would exist [6]. In fact, by corrugating the contact line, it is possible to find a pathway through which any equilibrium configuration can lower its energy. Against such results, some authors reply that perturbations of the contact line unavoidably involve perturbations of the free surface of the droplet that, in turn, increase the surface energy and so depress the destabilizing effect of line tension (see, e.g., [7] and p 237 of [8]). Appealing as these arguments might seem, they do not capture the essence of the problem: a line energy proportional to the length of the contact line, with a negative constant of proportionality, can always be made large and negative in a way that cannot be counterbalanced by reasonable surface terms: to achieve this goal it is sufficient to make the contact line wigglier and wigglier.

However, the soundness of this mathematical argument hides another crucial issue. The destabilizing feature of unstable modes is the high wavelength ℓ_m of the oscillations induced on the contact line. When ℓ_m becomes a microscopic length comparable with the thickness ℓ_c of the three-phase contact region that is replaced by the contact line in a continuum description, then the modes operate at a length scale where the continuum approach needs corrections by either adding curvature-dependent terms to line tension [9], or modelling the interaction with the substrate through an effective potential diluted in the bulk [10]. Thus, claims against negative values of the line tension are inappropriate until an estimate of ℓ_m is available: if ℓ_m is larger than ℓ_c, then the instability is effective where the continuum model is, and so it should be accounted for. But if ℓ_m is shorter than ℓ_c, unstable modes should be discarded as inconsistent with the continuum model. This issue has been raised recently in [11] for liquid filaments and in [12] for sessile droplets sitting on a flat substrate, where tentative estimates of ℓ_m have been proposed.

Here we consider the equilibrium of a spherical droplet of radius r sitting on a spherical substrate of radius R, by stressing the interplay between line tension and the substrate's curvature in determining the stability of equilibrium. Our method makes it possible to explore all meaningful values of R, from $R \gg r$ where our results reproduce those obtained in [12] for a flat substrate, to $R \ll r$, where we can complete the stability analysis performed in [5] and [13].

Besides the radius R of the substrate, two length scales of the problem are the ratio ξ between the line and the surface tension and the size $\sqrt[3]{3V/\pi}$ of the droplet expressed through its constant volume V. To appreciate the effects of constitutive parameters on equilibrium and

stability, we proceed by fixing two of them at a time. For instance, to focus on the effects of line tension, we can vary ξ and prescribe the geometry of the problem by fixing R and V. In section 2, after introducing the continuum model we adopt, we perform the equilibrium analysis. It turns out that a unique equilibrium configuration exists when the line tension is negative, whereas up to three equilibria exist for positive line tensions. This should be contrasted with the results of [13] where a spherical solid particle, acting as the substrate, lies at a *flat* interface between two liquids and so no constraint is placed on the volume of the (infinite) droplet. In that case, only two equilibria could exist, at most. Section 3 is devoted to stability analysis. After recalling the basic ingredients of the stability criterion we employ, we prove that for positive line tensions only one branch of solutions is stable until it merges with an unstable branch at a turning point, in accordance with the results of [5] and [13] obtained only by global stability arguments. The third branch, which was not considered in [5] and [13] and which exists regardless of the value of line tension, is always unstable. The analysis is easier to perform in terms of the equilibrium contact angle ϑ_c and of the dimensionless parameters $\varepsilon = \xi/r, \varrho = r/R$. The drawback of this procedure is that these parameters are not constitutive, but depend on the solution. To interpret the results in terms of constitutive parameters, we introduce a *reverse mapping* in section 4. We obtain two-dimensional bifurcation diagrams by using cross sections in the parameter space. According to the parameters that are held fixed, the results look different. When both the line tension and the substrate's radius are fixed, while the droplet's volume is free to vary, three different scenarios could occur, depending on the value of the bare contact angle ϑ_c^0, that is, the equilibrium contact angle when line tension is absent. When ϑ_c^0 is below a threshold ϑ_{cm}^0, stable equilibria exist provided that a droplet has neither a too large nor a too small volume. If $\vartheta_c^0 \in \left[\vartheta_{cm}^0, \vartheta_{cM}^0\right]$ stable equilibria exist only when the droplet's volume is large enough. Finally, if $\vartheta_c^0 > \vartheta_{cM}^0$ no stable equilibria survive for positive line tensions. It should be noted that both the critical values ϑ_{cm}^0 and ϑ_{cM}^0 depend on the substrate's curvature. Different regimes exist also when the geometric setting is prescribed by fixing $\Lambda := (3V/\pi)^{1/3}/R$. While for most values of Λ the bifurcation diagrams are qualitatively similar to those obtained for flat substrates, no stable equilibrium exists when Λ takes its values in a suitable range depending on the bare contact angle.

All these results hold when the line tension is positive. When it is negative, we can prove that the unique equilibrium solution is always unstable against modes that make the contact line more and more corrugated. As in [12], we introduce the index of residual stability m_{rs} associated with an equilibrium configuration: it is an integer that counts the number of *stable* modes. The higher is m_{rs}, the more we are confident that negative line tensions are reliable since high values of m_{rs} mean that the unstable modes require wild corrugations of the contact line to induce instability, and so they are likely to operate at length scales where the continuum approach employed here does not hold. As a result, we prove that the substrate's curvature somehow amplifies the destabilizing role of negative line tension since the reservoir of stable modes is depleted when the droplet sits on a curved substrate. This conclusion also leads to a critical examination of the results discussed in [5], since it proves that the fact that negative line tension reduces the energy of a sessile droplet at equilibrium does not assess its stability for which a local analysis such as that presented here is required.

To study global stability, first-order phase transitions should also be considered, by comparing the energy of a droplet sitting on the substrate with the energy of two particular configurations. The former, where the substrate and the droplet are both merged in the ambient fluid, but are detached from one another; the latter, where the substrate is wrapped by the droplet which, in turn, is merged within the ambient fluid. This study is sketched in section 5 along the lines of [5] and [13], but also accounting for finite-volume effects and

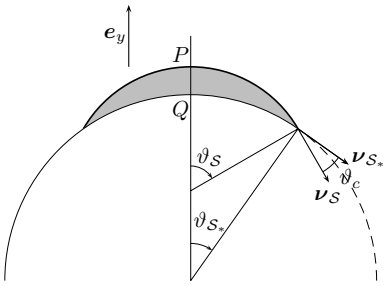

Figure 1. A sessile droplet (shaded region) sitting upon a spherical substrate. The contact angle ϑ_c is the angle between the conormal unit vectors $\boldsymbol{\nu}_{\mathcal{S}}$ and $\boldsymbol{\nu}_{\mathcal{S}_*}$ of the contact line, viewed as a curve on $\mathcal{S}$ and on $\mathcal{S}_*$, respectively.

Table 1. Synopsis of different notations. The suffixes lv, ls and sv employed, for instance, in [13] denote the liquid–vapour, the liquid–solid and the solid–vapour interfaces. The notation employed in [5] is tailored on the theory of emulsions where ow denotes the interface between the liquid phases of the emulsion, oil and water; sd stands for the interface between the solid particle and the dispersed phase, and sc denotes the interface between the solid particle and the continuous phase.

This paper	Reference [13]	Reference [5]
γ	γ_{lv}	γ_{ow}
w	$\gamma_{\mathrm{lv}} - \gamma_{\mathrm{ls}} + \gamma_{\mathrm{sv}}$	$\gamma_{\mathrm{ow}} - \gamma_{\mathrm{sd}} + \gamma_{\mathrm{sc}}$

stressing the role of curvature in making encapsulation or detachment of the droplet from the substrate energetically favoured. Finally, section 6 closes the paper with some summarizing remarks and five appendices contain technical details of the numerical procedures adopted in this paper.

2. Equilibria

Here we determine the equilibrium configurations of a sessile droplet $\mathcal{B}$ laid on a spherical substrate of radius R, as sketched in figure 1. The droplet $\mathcal{B}$ consists of incompressible fluid and so its volume has a fixed value V. The boundary $\partial\mathcal{B}$ of $\mathcal{B}$ can be split as $\partial\mathcal{B} = \mathcal{S} \cup \mathcal{S}_*$, where $\mathcal{S}$ is the *free* surface in contact with a third phase and $\mathcal{S}_*$ is the *adhering* surface, in contact with the solid substrate. The surfaces $\mathcal{S}$ and $\mathcal{S}_*$ meet along the *contact line* $\mathcal{C}$, a closed curve where three phases coexist at equilibrium. The simplest free-energy functional for this system is

$$\mathcal{F}[\mathcal{B}] = \gamma \int_{\mathcal{S}} \mathrm{d}a + (\gamma - w) \int_{\mathcal{S}_*} \mathrm{d}a + \tau \int_{\mathcal{C}} \mathrm{d}s, \tag{1}$$

where $\gamma > 0$ is the surface tension pertaining to the interface $\mathcal{S}$, $w > 0$ is the adhesion potential that measures the adhesive properties of the substrate, and τ is the line tension of $\mathcal{C}$ which, in principle, could be of either sign.

For the ease of the reader, in table 1 we compared our notation with those adopted in [13] and [5].

The free-energy functional (1) is the simplest functional that can account for line tension effects. Several simplifying assumptions are involved in (1), which we briefly discuss here. First, the surface tension γ is assumed to be constant and no curvature corrections like that introduced by Tolman [14] have been considered. By taking both w and τ constant, we are

making two assumptions. First, that the substrate is chemically homogeneous. Second, and more important, that the substrate's curvature does not affect the adhesion potential w and the line tension τ. As noted in [12], introducing terms in the energy that depend on the curvature of $\mathcal{S}, \mathcal{S}_*$ or $\mathcal{C}$ could modify the outcomes of the stability analysis, especially for negative line tensions. In fact, some preliminary results [15] show that curvature corrections to line tension increase the order of the differential operators entering the natural boundary conditions associated with the stability problem (see equation (4.10) of [16]). These corrections, which operate at a length scale smaller than the characteristic length $|\xi|$ taken here as a lower bound for our model, indicate that the destabilizing role of negative line tension is reduced, but still exists and depends on the parameters of the problem such as, for instance, the contact angle.

In (1) no bulk effects are accounted for, and so the equilibrium free surface $\mathcal{S}$ has constant mean curvature (see, e.g., [16]). This hypothesis amounts to considering droplets that are small enough to neglect gravity and also to neglecting the forces between the droplet and the substrate molecules that are effective in a narrow region close to $\mathcal{S}_*$. These forces enter the free-energy functional through a bulk term whose density is closely related to the disjoining forces [17, 18]. They modify the droplet's equilibrium profile in a region close to the contact line and might affect the Young equation along the contact line $\mathcal{C}$. For the stability analysis we have in mind, the first feature would lead to considerable technical complications, since a sphere would no longer solve the equilibrium equation, and so the spectral analysis contained in section 3 would be harder to accomplish in detail. Apart from this, since disjoining pressure does not modify dramatically the mathematical structure of the stability analysis, we expect it will modify its conclusions only quantitatively but not qualitatively. It remains true, however, that only a complete stability analysis including both curvature corrections and disjoining pressure could clarify this issue. Finally, while thermal fluctuations do not appear in (1), the stability analysis performed in section 3 can be interpreted in terms of thermal fluctuations: in fact, the perturbing modes affecting any equilibrium configurations can be conceived as having a thermal origin.

Line tension affects the boundary condition along $\mathcal{C}$ which generalizes the classical Young equation and reads as [16]

$$\gamma \cos \vartheta_c + \gamma - w - \tau \kappa_g^* = 0. \tag{2}$$

In (2), ϑ_c is the *contact angle*, the angle between the droplet's and the substrate's conormal unit vectors along $\mathcal{C}$ (see figure 1), and κ_g^* is the geodesic curvature of $\mathcal{C}$ viewed as a curve of $\mathcal{S}_*$. We also assume that the ratio $\frac{w-\gamma}{\gamma}$ ranges in $[-1, 1]$, so that a *bare* contact angle $\vartheta_c^0 \in [0, \pi]$ satisfying

$$\cos \vartheta_c^0 = \frac{w - \gamma}{\gamma} \tag{3}$$

can be defined: the angle ϑ_c^0 would be the contact angle at equilibrium, if the line tension were absent. The ratio

$$\xi := \frac{\tau}{\gamma} \tag{4}$$

has the same sign as the line tension and it will play a central role in the subsequent analysis, as $|\xi|$ sets the typical length scale of the model. Roughly speaking, $|\xi|$ is the size of a hypothetical droplet for which surface and line energies in (1) are comparable. Experimental data [19] suggest that ξ can be of either sign, with magnitude ranging between 10^{-8} and 10^{-6} m. Hereafter, we assume a conservative attitude by taking $\ell_c = |\xi|$, so that length scales shorter than $|\xi|$ are inaccessible to our model.

Among surfaces with constant mean curvature, here we focus on droplets $\mathcal{B}$ having a spherical cap of radius r as a free surface. The dimensionless ratio

$$\rho := \frac{r}{R} \tag{5}$$

will be frequently employed in what follows. The system formed by the droplet and the substrate is axially symmetric about the direction $\boldsymbol{e}_y$ shown in figure 1. The symmetry axis $\boldsymbol{e}_y$ intersects the free surface $\mathcal{S}$ at P, where the outward unit normal vector $\boldsymbol{\nu}$ of the droplet is $\boldsymbol{\nu}_P = \boldsymbol{e}_y$, and the adhering surface $\mathcal{S}_*$ at Q where the outward unit normal vector $\boldsymbol{\nu}_*$ is $\boldsymbol{\nu}_{*Q} = -\boldsymbol{e}_y$. Along the contact curve, the angle $\vartheta_{\mathcal{S}}$ between $\boldsymbol{\nu}$ and $\boldsymbol{\nu}_P$ and the angle $\vartheta_{\mathcal{S}_*}$ between $\boldsymbol{\nu}$ and $\boldsymbol{\nu}_{*Q}$ are constant. Simple geometric considerations yield

$$\begin{aligned} \vartheta_c &= \vartheta_{\mathcal{S}} - \vartheta_{\mathcal{S}_*} \\ \sin\vartheta_{\mathcal{S}} &= \frac{1}{\rho}\sin\vartheta_{\mathcal{S}_*} \end{aligned} \tag{6}$$

from which we obtain

$$\cos\vartheta_{\mathcal{S}} = \frac{\cos\vartheta_c - \rho}{\sqrt{1+\rho^2-2\rho\cos\vartheta_c}} \qquad \cos\vartheta_{\mathcal{S}_*} = \frac{1-\rho\cos\vartheta_c}{\sqrt{1+\rho^2-2\rho\cos\vartheta_c}}. \tag{7}$$

The geodesic curvatures of $\mathcal{C}$, viewed as a curve on either $\mathcal{S}$ or $\mathcal{S}_*$, are (see, e.g., p 249 of [20])

$$\kappa_g = \frac{(\rho-\cos\vartheta_c)}{r\sin\vartheta_c} \tag{8}$$

and

$$\kappa_g^* = \frac{(\rho\cos\vartheta_c - 1)}{r\sin\vartheta_c}, \tag{9}$$

respectively. To recast (2) in a dimensionless form, it is expedient to introduce the ratios

$$\varepsilon := \frac{\xi}{r} \qquad \text{and} \qquad \Xi := \frac{\xi}{R} \tag{10}$$

that change sign when the line tension does. We note that Ξ is a constitutive parameter while ε, like ϱ, depends on the actual solution through the droplet's radius r. Although in principle Ξ could be any real number, we confine ourselves to the range $|\Xi| < 1$, so that the radii of the substrate cannot be shorter than $R = |\xi|$. This is consistent with our view of $|\xi|$ as the shortest length scale accessible to the model. For future use, we note that, by equations (5) and (10),

$$\rho = \frac{\Xi}{\varepsilon}. \tag{11}$$

Finally, we introduce two more dimensionless parameters,

$$\tau^* := \frac{\xi}{\sqrt[3]{\frac{3V}{\pi}}}, \tag{12}$$

which compares ξ with the typical size of the droplet, and

$$\Lambda := \frac{\left(\frac{3V}{\pi}\right)^{1/3}}{R} = \frac{\Xi}{\tau^*}. \tag{13}$$

Prescribing Λ is the same as fixing the geometry of the substrate and the volume of the droplet, while the line tension is left free. On the other hand, when Ξ is prescribed, the geometry of the substrate and the line tension are held fixed whereas the volume of the droplet acts as a free parameter. Here, we first illustrate our analysis at fixed Ξ (Ξ-ensemble), and then we map the results at fixed Λ (Λ-ensemble) in the next subsection. To be consistent, we shall confine ourselves to the case $|\tau^*| < 1$, so that even the size of the droplet cannot be smaller than $|\xi|$.

2.1. Equilibrium in the Ξ-ensemble

By use of equations (3) and (9) we can write (2) as

$$\varepsilon(-1+\rho\cos\vartheta_c)=\sin\vartheta_c\big(\cos\vartheta_c-\cos\vartheta_c^0\big) \tag{14}$$

which can be solved to obtain ε as a function of the contact angle ϑ_c, parameterized by ϑ_c^0 and Ξ:

$$\varepsilon=\Theta\big(\vartheta_c\big|\vartheta_c^0,\,\Xi\big):=\cos\vartheta_c(\Xi-\sin\vartheta_c)+\cos\vartheta_c^0\sin\vartheta_c. \tag{15}$$

In (15), a bar separates the variable ϑ_c from the set of constitutive parameters ϑ_c^0 and Ξ on which Θ depends. As already remarked in the introduction, the droplet's volume has a constant value V. Viewing $\mathcal{B}$ as the set difference between two spherical caps of radii R and r, subtending angles $2\vartheta_{\mathcal{S}}$ and $2\vartheta_{\mathcal{S}_*}$ (see figure 1), it is not difficult to prove that

$$\frac{3V}{\pi r^3}=\frac{2+\rho^2+2\rho^4-2(\rho+\rho^3)\cos\vartheta_c-\rho^2\cos\vartheta_c^2}{\rho^3\sqrt{1+\rho^2-2\rho\cos\vartheta_c}}-\frac{2}{\rho^3}+2=:V(\vartheta_c,\rho), \tag{16}$$

where equations (7) have been used too. By recalling definitions $(10)_1$ and (12), we can solve (16) with respect to ε, obtaining

$$\varepsilon_*(\vartheta_c,\rho|\tau^*)=\mathcal{V}_*(\vartheta_c,\rho):=\tau^*\sqrt[3]{V(\vartheta_c,\rho)}. \tag{17}$$

Before solving equations (15) and (17), we note that when $\rho\cos\vartheta_c=1$, κ_g^* vanishes and so $\mathcal{C}$ is a geodesic curve of $\mathcal{S}_*$. Then, by (2), the line tension does not affect the equilibrium and the contact angle ϑ_c coincides with ϑ_c^0. Thus, $\rho=1/\cos\vartheta_c^0$ holds which, when replaced in (17), yields the relation among the constitutive parameters R, V and ϑ_c^0 in this special case:

$$\frac{3V}{\pi R^3}\equiv\Lambda^3=\frac{2-\cos^2\vartheta_c^0-\cos^4\vartheta_c^0+2\sin\vartheta_c^0\big(1-\cos^3\vartheta_c^0\big)}{\sin\vartheta_c^0\cos^3\vartheta_c^0}.$$

Finally, by (9), the contact line only wets the upper hemisphere of the substrate when $\rho\cos\vartheta_c<1$, while it also wets the lower hemisphere when $\rho\cos\vartheta_c>1$.

Let $\mathcal{P}:=\big\{\big(\vartheta_c^0,\tau^*,\Xi\big)\big\}$ be the set of constitutive parameters that parameterize the solutions of equations (15) and (17). Given a point $P\equiv\big(\vartheta_c^0,\tau^*,\Xi\big)$ in $\mathcal{P}$, any solution will be characterized by the set $(\vartheta_c,\varepsilon,\rho)$ that can be viewed as a point in a further set $\mathcal{G}$. To solve equations (15) and (17) we first introduce the function

$$f\big(\vartheta_c\big|\vartheta_c^0,\,\Xi\big):=\frac{\Xi}{\Theta\big(\vartheta_c\big|\vartheta_c^0,\,\Xi\big)} \tag{18}$$

which, by (11), is the effective value of ρ on the solution of (15). For a given point in $\mathcal{P}$, we subtract (17) from (15) and then use (18) to obtain

$$\Upsilon\big(\vartheta_c\big|\vartheta_c^0,\tau^*,\Xi\big):=\Theta\big(\vartheta_c\big|\vartheta_c^0,\,\Xi\big)-\mathcal{V}_*\big(\vartheta_c,\,f\big(\vartheta_c\big|\vartheta_c^0,\,\Xi\big)\big)=0. \tag{19}$$

The function f in (18) is defined when $\Theta\big(\vartheta_c\big|\vartheta_c^0,\,\Xi\big)\neq 0$. We expect that both $\mathcal{V}_*\big(\vartheta_c,\,f\big(\vartheta_c\big|\vartheta_c^0,\,\Xi\big)\big)$ and $\Upsilon\big(\vartheta_c\big|\vartheta_c^0,\tau^*,\,\Xi\big)$ have a jump at the points $\bar\vartheta_c$ where $\Theta\big(\vartheta_c\big|\vartheta_c^0,\,\Xi\big)$ vanishes. In fact, let us suppose that $\Xi>0$ and that $\bar\vartheta_c$ is the smallest, simple zero of $\Theta\big(\vartheta_c\big|\vartheta_c^0,\,\Xi\big)$: minor adjustments are required to cover other cases. Since $\Theta\big(0\big|\vartheta_c^0,\,\Xi\big)=\Xi>0$, we conclude that

$$\lim_{\vartheta_c\to\bar\vartheta_c^{\mp}}f\big(\vartheta_c\big|\vartheta_c^0,\,\Xi\big)=\pm\infty$$

and so, by (16),

$$\lim_{\vartheta_c\to\bar\vartheta_c^{-}}\mathcal{V}_*\big(\vartheta_c,\,f\big(\vartheta_c\big|\vartheta_c^0,\,\Xi\big)\big)=\tau^*\sqrt[3]{4}\qquad\text{and}\qquad\lim_{\vartheta_c\to\bar\vartheta_c^{+}}\mathcal{V}_*\big(\vartheta_c,\,f\big(\vartheta_c\big|\vartheta_c^0,\,\Xi\big)=0,$$

from which the result follows. The point $\bar{\vartheta}_c$, however, solves (19) only for the triple $\left(\vartheta_c^0, 0, \Xi\right)$ that is, by (12), when the line tension vanishes, since only in that case $\varepsilon = 0$ also solves (17) for finite values of V.

To study how the zeroes of $\Upsilon\left(\vartheta_c \middle| \vartheta_c^0, \tau^*, \Xi\right)$ depend on τ^* we fix the parameters Ξ and ϑ_c^0 and note that, by definition,

$$\lim_{\vartheta_c \to 0^+} \Theta\left(\vartheta_c \middle| \vartheta_c^0, \Xi\right) = \lim_{\vartheta_c \to 0^+} \Upsilon\left(\vartheta_c \middle| \vartheta_c^0, \tau^*, \Xi\right) = \Xi, \tag{20}$$

$$\lim_{\vartheta_c \to \pi} \Theta\left(\vartheta_c \middle| \vartheta_c^0, \Xi\right) = -\Xi, \tag{21}$$

$$\lim_{\vartheta_c \to \pi} \Upsilon\left(\vartheta_c \middle| \vartheta_c^0, \tau^*, \Xi\right) = -\Xi - \tau^* \sqrt[3]{4}, \tag{22}$$

$$\lim_{\tau^* \to 0} \Upsilon\left(\vartheta_c \middle| \vartheta_c^0, \tau^*, \Xi\right) = \Theta\left(\vartheta_c \middle| \vartheta_c^0, \Xi\right), \tag{23}$$

and

$$\lim_{\vartheta_c \to 0^+} \frac{\mathrm{d}\Theta\left(\vartheta_c \middle| \vartheta_c^0, \Xi\right)}{\mathrm{d}\vartheta_c} = \cos \vartheta_c^0 - 1 \leqslant 0. \tag{24}$$

It is possible to verify that the continuous function $\Theta\left(\vartheta_c \middle| \vartheta_c^0, \Xi\right)$ has, at most, one local maximum and one local minimum in the set $(0, \pi)$,

$$\Theta_m\left(\vartheta_c^0, \Xi\right) := \min_{(0,\pi)} \Theta\left(\vartheta_c \middle| \vartheta_c^0, \Xi\right) \qquad \text{and} \qquad \Theta^M(\vartheta_c^0, \Xi) := \max_{(0,\pi)} \Theta\left(\vartheta_c \middle| \vartheta_c^0, \Xi\right).$$

When these critical points exist, we call ϑ_c^m and ϑ_c^M the values of ϑ_c where $\Theta\left(\vartheta_c \middle| \vartheta_c^0, \Xi\right)$ attains them,

$$\Theta_m\left(\vartheta_c^0, \Xi\right) = \Theta\left(\vartheta_c^m \middle| \vartheta_c^0, \Xi\right), \qquad \Theta^M\left(\vartheta_c^0, \Xi\right) = \Theta\left(\vartheta_c^M \middle| \vartheta_c^0, \Xi\right). \tag{25}$$

By equations (20) and (24), it follows that $\vartheta_c^m < \vartheta_c^M$. Moreover, the function $\Upsilon\left(\vartheta_c \middle| \vartheta_c^0, \tau^*, \Xi\right)$ also attains, at most, one local minimum $\Upsilon^m\left(\vartheta_c^0, \tau^*, \Xi\right)$ and one local maximum $\Upsilon^M\left(\vartheta_c^0, \tau^*, \Xi\right)$ in $(0, \pi)$ at points whose distance from ϑ_c^m and ϑ_c^M, respectively, depends on τ^*. To avoid clutter, in what follows we shall only stress the dependence of Υ^m and Υ^M on τ^* by setting $\Upsilon^m(\tau^*) := \Upsilon^m\left(\vartheta_c^0, \tau^*, \Xi\right)$ and $\Upsilon^M(\tau^*) := \Upsilon^M\left(\vartheta_c^0, \tau^*, \Xi\right)$. We also call $\bar{\vartheta}_c^{(i)}$ the ith zero of $\Theta\left(\vartheta_c \middle| \vartheta_c^0, \Xi\right)$, where i is strictly positive, as follows from equations (20), (21), and the continuity of $\Theta\left(\vartheta_c \middle| \vartheta_c^0, \Xi\right)$. Finally, let us introduce the functions $\tau_c^{*m}\left(\vartheta_c^0, \Xi\right)$ and $\tau_c^{*M}\left(\vartheta_c^0, \Xi\right) > \tau_c^{*m}\left(\vartheta_c^0, \Xi\right)$ such that

$$\Upsilon^m\left(\tau_c^{*m}\left(\vartheta_c^0, \Xi\right)\right) = 0 \qquad \text{and} \qquad \Upsilon^M\left(\tau_c^{*M}\left(\vartheta_c^0, \Xi\right)\right) = 0.$$

Since we do not have an analytic expression for $\tau_c^{*m}\left(\vartheta_c^0, \Xi\right)$ and $\tau_c^{*M}\left(\vartheta_c^0, \Xi\right)$, we compute them through a numerical algorithm illustrated in appendix A. At fixed $0 < \Xi < 1$, the function $\tau_c^{*m}\left(\vartheta_c^0, \Xi\right)$ tends to zero when $\vartheta_c^0 \to \theta_{c1}^0$, with θ_{c1}^0 satisfying $\Theta_m\left(\vartheta_c \middle| \theta_{c1}^0, \Xi\right) = 0$. Similarly, the function $\tau_c^{*M}\left(\vartheta_c^0, \Xi\right)$ tends to zero when $\vartheta_c^0 \to \theta_{c2}^0$, satisfying $\Theta^M\left(\vartheta_c \middle| \theta_{c2}^0, \Xi\right) = 0$. Finally, when $\Xi = 1$, $\theta_{c1}^0 \equiv \theta_{c2}^0 = \pi/2$ and the maximum and the minimum of $\Theta\left(\vartheta_c \middle| \vartheta_c^0, \Xi\right)$ merge into an inflection point.

After these general remarks, we now show that for positive line tensions (19) has a number of zeroes varying from one to three, depending on the values of τ^*. Hereafter, we examine different cases: the reader can also follow the discussion by looking at figure 2.

(i) $\Theta_m\left(\vartheta_c^0, \Xi\right) > 0$, $\tau^* \in \left[0, \tau_c^{*m}\left(\vartheta_c^0, \Xi\right)\right)$. The curves $\Upsilon\left(\vartheta_c \middle| \vartheta_c^0, \tau^*, \Xi\right)$ move downwards from $\Theta\left(\vartheta_c \middle| \vartheta_c^0, \Xi\right)$ maintaining both $\Upsilon^m(\tau^*)$ and $\Upsilon^M(\tau^*)$ positive. Equation (19) has a unique root $p_3(\tau^*) \in \left(\vartheta_c^M, \pi\right)$.

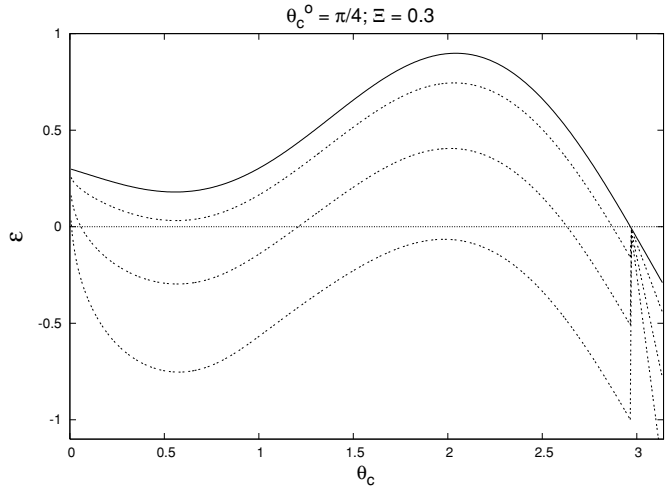

Figure 2. Graphs of $\Theta(\vartheta_c|\vartheta_c^0, \Xi)$ (solid curve) and $\Upsilon(\vartheta_c|\vartheta_c^0, \tau^*, \Xi)$, for three values of τ^*, in the $(\vartheta_c, \varepsilon)$ plane. When $\vartheta_c^0 = \frac{\pi}{4}$ and $\Xi = 0.3$ we chose, from top to bottom, $\tau^* = 0.1, 0.32, 0.63$ to illustrate the cases where $\tau^* < \tau_c^{*m}(\vartheta_c^0, \Xi)$, $\tau_c^{*m}(\vartheta_c^0, \Xi) < \tau^* < \tau_c^{*M}(\vartheta_c^0, \Xi)$ and $\tau^* > \tau_c^{*M}(\vartheta_c^0, \Xi)$, respectively. In the first and third cases (19) has only one zero, while in the second case three distinct zeroes exist.

(ii) $\Theta_m\left(\vartheta_c^0, \Xi\right) > 0$, $\tau^* \in \left[\tau_c^{*m}\left(\vartheta_c^0, \Xi\right), \tau_c^{*M}\left(\vartheta_c^0, \Xi\right)\right]$. The minimum $\Upsilon^m(\tau^*)$ of $\Upsilon\left(\vartheta_c\middle|\vartheta_c^0, \tau^*, \Xi\right)$ is now negative, while $\Upsilon^M(\tau^*)$ is still positive. By equations (20) and (22), three distinct roots $p_1(\tau^*) \leqslant p_2(\tau^*) \leqslant p_3(\tau^*)$ of (19) exist, with $p_1(\tau^*) = p_2(\tau^*)$ at $\tau^* = \tau_c^{*m}\left(\vartheta_c^0, \Xi\right)$, and $p_2(\tau^*) = p_3(\tau^*)$ at $\tau^* = \tau_c^{*M}\left(\vartheta_c^0, \Xi\right)$.

(iii) $\Theta_m\left(\vartheta_c^0, \Xi\right) > 0$, $\tau^* > \tau_c^{*M}\left(\vartheta_c^0, \Xi\right)$. Both $\Upsilon^m(\tau^*)$ and $\Upsilon^M(\tau^*)$ are negative and (19) has a unique root $p_1(\tau^*) \in \left(0, \vartheta_c^m\right)$.

Hence, when the line tension is positive, there are two surfaces $\tau^* = \tau_c^{*M}\left(\vartheta_c^0, \Xi\right)$ and $\tau^* = \tau_c^{*m}\left(\vartheta_c^0, \Xi\right)$ in $\mathcal{P}$ such that three equilibria exist if $\tau^* \in \left(\tau_c^{*m}\left(\vartheta_c^0, \Xi\right), \tau_c^{*M}\left(\vartheta_c^0, \Xi\right)\right)$, while a unique equilibrium configuration exists, if either $\tau^* < \tau_c^{*m}\left(\vartheta_c^0, \Xi\right)$ or $\tau^* > \tau_c^{*M}\left(\vartheta_c^0, \Xi\right)$.

Since $\Upsilon\left(\vartheta_c\middle|\vartheta_c^0, \tau^*, \Xi\right)$ is continuous in any interval bounded by successive zeroes of $\Theta\left(\vartheta_c\middle|\vartheta_c^0, \Xi\right)$, the procedure just shown also works when $\Theta_m\left(\vartheta_c\middle|\vartheta_c^0, \Xi\right) < 0$, regardless of the sign of $\Theta_M\left(\vartheta_c\middle|\vartheta_c^0, \Xi\right)$:

(i) $\Theta_m\left(\vartheta_c^0, \Xi\right) < 0$, $\Theta_M\left(\vartheta_c^0, \Xi\right) > 0$, $\tau^* \in \left[0, \tau_c^{*M}\left(\vartheta_c^0, \Xi\right)\right]$. Equation (19) has three distinct roots $p_1(\tau^*) < p_2(\tau^*) \leqslant p_3(\tau^*)$, with $p_2(\tau^*) = p_3(\tau^*)$ at $\tau^* = \tau_c^{*M}\left(\vartheta_c^0, \Xi\right)$.

(ii) $\Theta_m\left(\vartheta_c^0, \Xi\right) < 0$, $\Theta_M\left(\vartheta_c^0, \Xi\right) > 0$, $\tau^* > \tau_c^{*M}\left(\vartheta_c^0, \Xi\right)$. Only the root $p_1(\tau^*) \in \left(0, \vartheta_c^m\right)$ of (19) survives.

(iii) $\Theta_m\left(\vartheta_c^0, \Xi\right) < 0$, $\Theta_M\left(\vartheta_c^0, \Xi\right) < 0$. Only $p_1(\tau^*) \in \left(0, \vartheta_c^m\right)$ solves (19), regardless of the value of τ^*.

In figure 3 we plotted graphs of $\log_{10}\tau_c^{*m}\left(\vartheta_c^0, \Xi\right)$ and $\log_{10}\tau_c^{*M}\left(\vartheta_c^0, \Xi\right)$ at different constant values of Ξ to appreciate the effects of the substrate's curvature on the equilibrium configurations. In the limit where $\Xi = 0$, the substrate is flat and the results coincide with those obtained in [12], $\tau_c^{*m}\left(\vartheta_c^0, 0\right) \equiv 0$, while $\tau_c^{*M}\left(\vartheta_c^0, 0\right)$ tends to the curve separating a region where two equilibria exist from a region where no equilibrium exists. The root $p_1(\tau^*)$ tends to $(0, 0, 0)$, which is a spurious solution already found in [12].

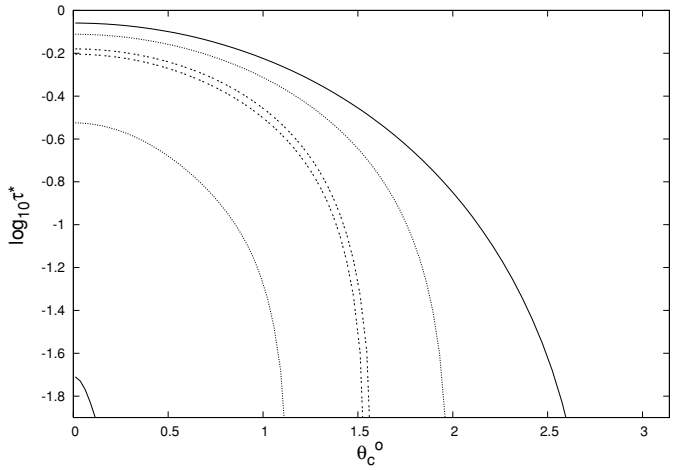

Figure 3. The curves plotted here are cross sections at constant Ξ of the surfaces $\log_{10}\tau_c^{*M}(\vartheta_c^0, \Xi)$ and $\log_{10}\tau_c^{*m}(\vartheta_c^0, \Xi)$: $\Xi = 0.01$ (solid, thick lines), $\Xi = 0.3$ (dotted lines) and $\Xi = 0.9$ (dashed lines). For any fixed Ξ, three equilibria exist in the region between the two curves, whereas only one equilibrium configuration survives elsewhere.

If the line tension is negative, by use of equations (20)–(23) it follows that

$$\Theta\left(\vartheta_c^m \middle| \vartheta_c^0, \Xi\right) < \Upsilon\left(\vartheta_c^m \middle| \vartheta_c^0, \tau^*, \Xi\right) < \Upsilon\left(0 \middle| \vartheta_c^0, \tau^*, \Xi\right) = \Theta\left(0 \middle| \vartheta_c^0, \Xi\right) = \Xi < 0$$

and

$$\Theta^M\left(\vartheta_c^0, \Xi\right) > 0$$

by which we conclude that a root $\bar{\vartheta}_c^{(1)}$ of $\Theta\left(\vartheta_c \middle| \vartheta_c^0, \Xi\right)$ exists for any choice of ϑ_c^0 and Ξ. Since now $\Upsilon\left(\vartheta_c \middle| \vartheta_c^0, \tau^*, \Xi\right) > \Theta\left(\vartheta_c \middle| \vartheta_c^0, \Xi\right)$ we conclude that (19) has a root in $\left(0, \bar{\vartheta}_c^{(1)}\right)$, regardless of the values of ϑ_c^0 and Ξ. This root is unique, since $\Theta\left(\vartheta_c \middle| \vartheta_c^0, \Xi\right)$ does not vanish elsewhere, as figure 4 illustrates.

2.2. Equilibrium in the Λ-ensemble

To study the effects of line tension on the equilibrium we rephrase the results just obtained in the Λ-ensemble, where Ξ is varied at constant Λ. Different scenarios are predicted, according to the values of the bare contact angle, whether it exceeds $\pi/2$ or not. In figure 5 E_{123}, E_1, and E_3 denote the regions where either three equilibria exist or a unique equilibrium—p_1 or p_3, respectively—exists. In what follows, we refer to the curves separating E_{123} from either E_1 or E_3 as to the E_1- or the E_3-curve. Finally, we refer to the locus where Λ is constant as to the Λ-curve. If the bare contact is larger than $\pi/2$ (see figure 5(b), where $\vartheta_c^0 = 9\pi/16$), we always pass from E_{123} to E_1 when line tension increases. When $\vartheta_c^0 < \pi/2$ (see figures 5(a) and 6, where $\vartheta_c^0 = 7\pi/16$ and $\pi/3$, respectively) different scenarios occur, depending on the value of Λ.

(i) $\Lambda > \Lambda_0\left(\vartheta_c^0\right) := 1/\tau_c^{*m}$. The Λ-curve intersects the E_3-curve once: on increasing Ξ, we pass from E_{123} to E_3 (figure 5(a)).
(ii) $\Lambda = \Lambda_0\left(\vartheta_c^0\right)$. A further intersection between the Λ- and the E_3-curve emerges at $\Xi = 1$.
(iii) $\Lambda_1\left(\vartheta_c^0\right) < \Lambda < \Lambda_0\left(\vartheta_c^0\right)$ (see figure 6(a)). The Λ- and the E_3-curve intersect each other twice when $\Xi < 1$. Then, on increasing Ξ towards 1 we pass from E_{123} to E_3 and back to E_{123}.

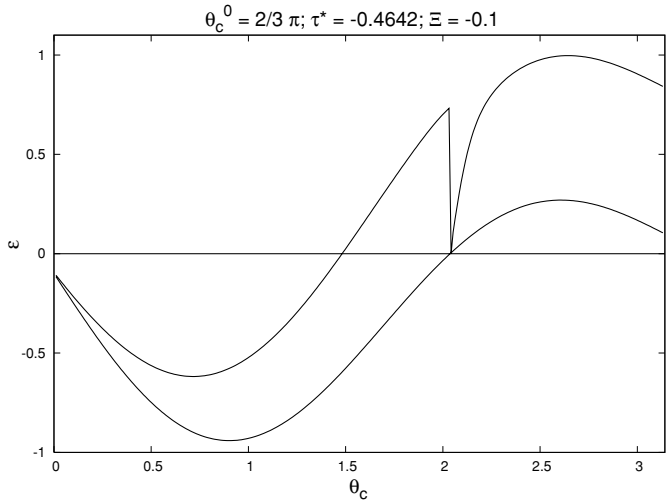

Figure 4. The functions $\Upsilon(\vartheta_c|\frac{2\pi}{3}, -0.4642, -0.1)$ and $\Theta(\vartheta_c|\frac{2\pi}{3}, -0.4642)$ are plotted against ϑ_c. Equation (19) has now a unique root, for all $\vartheta_c^0 \in (0, \pi)$ and $\Xi < 0$.

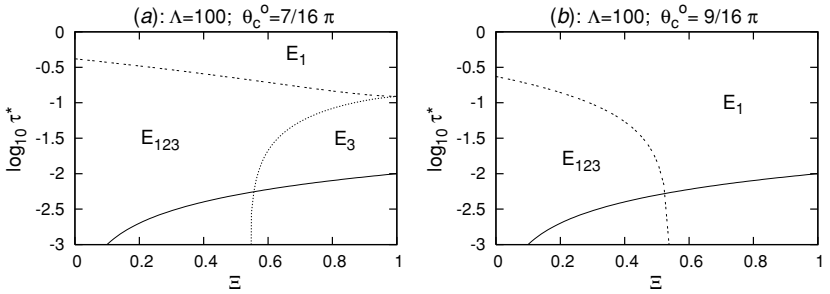

Figure 5. In (a) we plotted graphs of $\log_{10}\tau_c^{*m}(7\pi/16, \Xi)$ (dotted curve) and $\log_{10}\tau_c^{*M}(7\pi/16, \Xi)$ (dashed curve). In (b), where $\vartheta_c^0 = 9\pi/16$, only $\log_{10}\tau_c^{*M}(9\pi/16, \Xi)$ (dashed curve) has been plotted since $\tau_c^{*m}(\cdot, \Xi)$ never crosses the line at constant $\vartheta_c^0 > \pi/2$, as can be seen from figure 3. In the region E_{123}, three equilibria exist, in E_1 only the equilibrium $p_1(\tau^*)$ exists and in E_3 only the equilibrium $p_3(\tau^*)$ exists. The solid curve is the set where $\Lambda = 100$. On moving along this curve all geometric parameters are held fixed and we can study the effects of line tension on the equilibrium. On increasing line tension we move from E_{123} to E_3 in case (a) and to E_1 in case (b). If Λ is small enough, we can move to E_1 even if $\vartheta_c^0 < \pi/2$ (see figure 6).

(iv) $\Lambda = \Lambda_1(\vartheta_c^0) := 1/\tau_c^{*m}$. The Λ-curve intersects the E_1-curve at $\Xi = 1$.

(v) $\Lambda_c(\vartheta_c^0) < \Lambda < \Lambda_1(\vartheta_c^0)$ (see figure 6(b)). Besides two intersections with the E_3-curve, the Λ-curve also intersects the E_1-curve at $\Xi < 1$. Now, on increasing Ξ from 0 to 1 we pass from E_{123} to E_3 back to E_{123} and, finally, to E_1.

(vi) $\Lambda = \Lambda_c(\vartheta_c^0)$ (see figure 6(c)). The Λ-curve is tangent to the E_3-curve at a point where, in turn, two distinct equilibria exist. Apart from this point, we remain in E_{123} until we enter the E_1 region.

(vii) $\Lambda < \Lambda_c(\vartheta_c^0)$ (see figure 6(d)). The Λ-curve only intersects the E_1-curve and so we pass from E_{123} to E_1 as Ξ increases from 0 to 1.

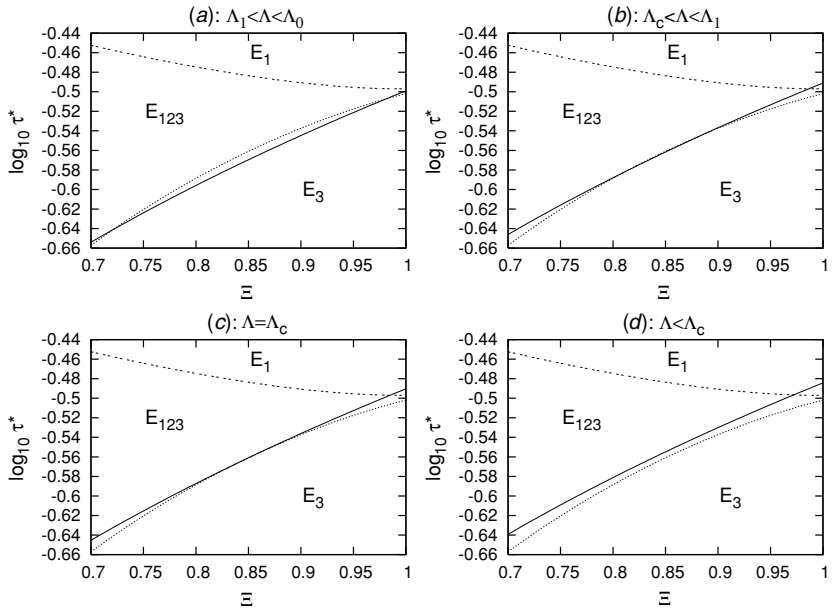

Figure 6. Graphs of $\log_{10}\tau_c^{*M}(\pi/3, \Xi)$ (dotted line) and $\log_{10}\tau_c^{*m}(\pi/3, \Xi)$ (dashed line) have been plotted here. The solid line is the set where $\Lambda = 3.155\,(a), 3.105\,(b), 3.09296\,(c), 3.05\,(d)$, respectively. This figure shows the scenarios outlined in the text when $\vartheta_c^0 < \pi/2$ and Λ is sufficiently small.

We stress that the complex scenario outlined here holds only when Λ ranges in a narrow interval $[\Lambda_c, \Lambda_0]$: in the case where $\vartheta_c^0 = \pi/3$, $\Lambda_0 \simeq 3.177$, $\Lambda_1 \simeq 3.14$ and $\Lambda_c \simeq 3.093$. The value of Λ_c is $O(1)$ for all values of $\vartheta_c^0 < \pi/2$, so that the droplet and the substrate size are comparable. Moreover, the reentrant transition from E_{123} to E_3 occurs at Ξ close to 1, which means that both R and $\sqrt[3]{3\pi/V}$ are comparable with ξ, and so quite small. We also note that, while computing Λ_0 is not difficult, arriving at Λ_c is a non-trivial task since no analytic expression for τ_c^{*M} exists. The strategy followed to arrive at Λ_c is outlined in appendix B. The regimes displayed here give rise to different bifurcation diagrams that we will study in section 4.

3. Stability

In this section we apply the criterion proposed in [16] to determine the local stability of the equilibrium configurations just found. The analysis extends that applied in [12] to sessile droplets laid on a flat substrate. In [16], the sign of the second variation of $\mathcal{F}$ was determined by finding the sign of the smallest eigenvalue μ of a differential operator. As a first step, the second variation $\delta^2\mathcal{F}$ of $\mathcal{F}$ is minimized on the set

$$\int_{\mathcal{S}} u^2 \,\mathrm{d}a = 1, \tag{26}$$

where u is the component of a perturbation field along the unit normal vector $\boldsymbol{\nu}$ of $\mathcal{S}$. Moreover, to enforce the incompressibility of the droplet, u should also obey the constraint

$$\int_{\mathcal{S}} u \,\mathrm{d}a = 0. \tag{27}$$

The integral constraints (26) and (27) are then added to $\delta^2\mathcal{F}$ by introducing two Lagrange multipliers $-\mu/2$ and λ. The Euler equation for the auxiliary functional

$$F[u] := \frac{1}{2}\int_{\mathcal{S}} \{|\nabla_s u|^2 + \alpha u^2\}\,\mathrm{d}a + \lambda\int_{\mathcal{S}} u\,\mathrm{d}a - \frac{1}{2}\mu\int_{\mathcal{S}} u^2\,\mathrm{d}a + \frac{1}{2}\int_{\mathcal{C}} \left\{\xi u_{s*}'^2 - \beta u_{s*}^2\right\}\mathrm{d}s \tag{28}$$

is then determined. In (28), a prime stands for differentiation with respect to the arc-length s on $\mathcal{C}$, u_{s*} is related to u through

$$u_{s*} = \frac{u}{\sin\vartheta_c},$$

and the function

$$\alpha := 2K - H^2 \tag{29}$$

depends on the total curvature H and on the Gaussian curvature K of $\mathcal{S}$. Finally,

$$\gamma\beta := \tau\left(K^* + \kappa_g^{*2}\right) + \gamma[H^*\sin\vartheta_c + H\cos\vartheta_c\sin\vartheta_c + \kappa_g\sin^2\vartheta_c] \tag{30}$$

where κ_g and κ_g^* are the geodesic curvatures of the contact line $\mathcal{C}$, as a curve embedded in either $\mathcal{S}$ or $\mathcal{S}_*$. Due to the different convexities of $\mathcal{S}$ and $\mathcal{S}_*$ we have $H = 2/r$ and $H^* = -2/R$. Moreover, $K = 1/r^2$ and $K^* = 1/R^2$. By use of equations (8)–(9), after some algebraic manipulations we can write the Euler equation for the functional F as

$$\Delta_s u + \left(\mu + \frac{2}{R^2}\right)u = \lambda \quad \text{on } \mathcal{S}, \tag{31}$$

together with the natural boundary condition

$$\left(\frac{\partial u}{\partial\vartheta} - \frac{\varepsilon}{\sin\vartheta_c^2\sin\vartheta^2}\frac{\partial^2 u}{\partial\varphi^2} - \frac{1}{\sin\vartheta_c^2}\left(\varepsilon\rho^2 + \varepsilon\left(\frac{1-\rho\cos\vartheta_c}{\sin\vartheta_c}\right)^2 + (\cos\vartheta_c - \rho)\sin\vartheta_c\right)u\right)\Bigg|_{\vartheta=\vartheta_S} = 0 \quad \text{along } \mathcal{C}, \tag{32}$$

where Δ_s is the Laplace–Beltrami operator on $\mathcal{S}$ that can be expressed in terms of the colatitude $\vartheta \in [0, \vartheta_S]$ and the azimuthal angle $\varphi \in [0, 2\pi)$ on $\mathcal{S}$ as

$$\Delta_s := \frac{1}{R^2}\frac{\partial^2}{\partial\vartheta^2} + \frac{1}{R^2}\cot\vartheta\frac{\partial}{\partial\vartheta} + \frac{1}{(R\sin\vartheta)^2}\frac{\partial^2}{\partial\varphi^2}. \tag{33}$$

The crucial point of the method is that the smallest eigenvalue $\mu_{\min}$ of the problem (31)–(32) coincides with the minimum of $\delta^2\mathcal{F}$ on the set (26). Hence, whenever $\mu_{\min}$ is positive on an equilibrium configuration, this latter is locally stable, while it is unstable when $\mu_{\min} < 0$. By retracing the steps of [12], we perform a modal analysis by first considering the homogeneous equation

$$\Delta_s\overline{u} + (\mu + 2)\overline{u} = 0 \quad \text{on } \mathcal{S} \tag{34}$$

and then setting

$$\overline{u} = \sum_{m=0}^{\infty} a_m u_m(\vartheta)\,\mathrm{trig}(m\varphi), \tag{35}$$

where

$$\mathrm{trig}(m\varphi) := \begin{cases} \sin(m\varphi) \text{ or } \cos(m\varphi) & \text{if } m \neq 0 \\ 1 & \text{if } m = 0, \end{cases}$$

and $a_m \in \mathbb{R}$ are the coefficients of the expansion. In (34), the factor R^{-2} in front of Δ_s has been dropped by rescaling μ to R^2. By inserting expansion (35) into (34) we conclude that,

for every value of m, the function $u_m(\vartheta)$ solves the equation

$$\frac{1}{\sin\vartheta}\frac{\mathrm{d}}{\mathrm{d}\vartheta}\left[\sin\vartheta\,\frac{\mathrm{d}u_m}{\mathrm{d}\vartheta}\right]+\left[\mu+2-\left(\frac{m}{\sin\vartheta}\right)^2\right]u_m=0. \tag{36}$$

The solution of (36) that is bounded everywhere on $\mathcal{S}$ is the associated Legendre function of the first kind $P_\nu^m(\cos\vartheta)$ (see, e.g., chapter 7 of [21]), where the index ν is related to μ by

$$\nu(\nu+1)=\mu+2. \tag{37}$$

As explained in [12], to guarantee that μ is real, the complex values of ν should obey either

$$\mathrm{Im}(\nu)=0 \qquad \text{or} \qquad \mathrm{Re}(\nu)=-\tfrac{1}{2}.$$

Moreover, without lack of generality, it is possible to consider only values of ν with imaginary part $\mathrm{Im}(\nu)\geqslant 0$ and real part $\mathrm{Re}(\nu)\geqslant -\frac{1}{2}$. Thus, ν ranges in the set

$$\mathcal{I}:=\left\{\nu\in\left[-\tfrac{1}{2}+\mathrm{i}0,\,-\tfrac{1}{2}+\mathrm{i}\infty\right)\cup\left[-\tfrac{1}{2},\,+\infty\right)\right\}$$

of the complex ν-plane. Modes with ν in the subset

$$\mathcal{U}:=\left\{\nu\in\left[-\tfrac{1}{2}+\mathrm{i}0,\,-\tfrac{1}{2}+\mathrm{i}\infty\right)\cup\left[-\tfrac{1}{2},\,1\right)\right\}$$

are *unstable* as they correspond, by (37), to negative values of μ. The solution u of (31) with λ rescaled to R^2 differs from $\overline{u}$ by a constant c related to the multipliers λ and μ through

$$(\mu+2)c=\nu(\nu+1)c=\lambda, \tag{38}$$

provided that $\mu\neq -2$ or, equivalently, $\nu\neq 0$. The function u also satisfies

$$\int_0^{\vartheta_c}\int_0^{2\pi}u(\vartheta,\varphi)\sin\vartheta\,\mathrm{d}\vartheta\,\mathrm{d}\varphi=0 \tag{39}$$

to obey the incompressibility constraint (27). In a modal analysis, where conditions are sought that make a specific mode unstable, the constraint (39) is adjusted mode by mode, by adding to the function

$$u_m(\vartheta,\varphi):=P_\nu^m(\cos\vartheta)\,\mathrm{trig}(m\varphi) \qquad m\in\mathbb{N} \tag{40}$$

a constant $c(\vartheta_{\mathcal{S}},\nu,m)$ that makes (39) satisfied, so that λ follows from (38) for all ν but $\nu=0$, a case that needs a separate treatment. By repeating *verbatim* the analysis of section 3 in [12] it is possible to prove that

$$c(\vartheta_{\mathcal{S}},\nu,m):=\begin{cases}0 & \text{if} \quad m\neq 0\\ -\dfrac{\cos\vartheta_{\mathcal{S}}P_\nu(\cos\vartheta_{\mathcal{S}})-P_{\nu+1}(\cos\vartheta_{\mathcal{S}})}{(1-\cos\vartheta_{\mathcal{S}})\nu} & \text{if} \quad m=0.\end{cases} \tag{41}$$

By fixing m, and replacing u with $P_\nu^m(\cos\vartheta)\,\mathrm{trig}(m\varphi)$ in (32), we arrive at the following expression for ε as a function of ϑ_c and ρ, parameterized by ν and m

$$\varepsilon_\nu^m(\vartheta_c,\rho)=(\sin\vartheta_c)^3\begin{cases}\dfrac{(\rho-\cos\vartheta_c)(P_\nu(\cos\vartheta_{\mathcal{S}})+c(\nu,\vartheta_{\mathcal{S}}))+\sin\vartheta_c\frac{\partial P_\nu(\cos\vartheta)}{\partial\vartheta}\big|_{\vartheta=\vartheta_{\mathcal{S}}}}{(1+\rho^2-2\rho\cos\vartheta_c)(P_\nu(\cos\vartheta_{\mathcal{S}})+c(\nu,\vartheta_{\mathcal{S}}))}, & m=0\\ \dfrac{(\rho-\cos\vartheta_c)P_\nu^m(\cos\vartheta_{\mathcal{S}})+\sin\vartheta_c\frac{\partial P_\nu^m(\cos\vartheta)}{\partial\vartheta}\big|_{\vartheta=\vartheta_{\mathcal{S}}}}{\left[\rho^2-2\rho\cos\vartheta_c-m^2\left(\frac{\sin\vartheta_c}{\sin\vartheta_{\mathcal{S}}}\right)^2+1\right]P_\nu^m(\cos\vartheta_{\mathcal{S}})}, & m\geqslant 2.\end{cases} \tag{42}$$

In (42), the value $m = 1$ has been ruled out. In fact, when $P_\nu^1(\cos\vartheta)\,\mathrm{trig}\,(\varphi)$ is inserted into (32), the coefficient in front of ε vanishes identically and (32) has no solution if $\nu \neq 1$, while it is identically satisfied in ϑ_c and ρ, if $\nu = 1$. This is not surprising, since the function $P_1^1(\cos\vartheta)\,\mathrm{trig}\,\varphi$ is the component, orthogonal to $\mathcal{S}$, of a rotation of $\mathcal{B}$ about the axis $\boldsymbol{e}_z$ or $\boldsymbol{e}_x$, orthogonal to $\boldsymbol{e}_y$ in figure 1, and so it is an infinitesimal rigid motion of the droplet along the substrate. Hence, this mode does not modify the energy of the droplet and, by (37), it consistently corresponds to $\mu = 0$. In general, modes with $\mu = 0$ will be referred to as the *marginal* modes.

We also note that (42) is not defined when $\nu = n_0$, where n_0 is an integer smaller than m, since $P_{n_0}^m(\cdot) \equiv 0$. However, we can rewrite $(42)_2$ as

$$\varepsilon_\nu^m(\vartheta_c, \varrho) = \frac{(\rho - \cos\vartheta_c)}{\left[\rho^2 - 2\rho\cos\vartheta_c - m^2\left(\frac{\sin\vartheta_c}{\sin\vartheta_S}\right)^2 + 1\right]} + \frac{\sin\vartheta_c \frac{\partial P_\nu^m(\cos\vartheta)}{\partial\vartheta}\Big|_{\vartheta=\vartheta_S}}{\left[\rho^2 - 2\rho\cos\vartheta_c - m^2\left(\frac{\sin\vartheta_c}{\sin\vartheta_S}\right)^2 + 1\right] P_\nu^m(\cos\vartheta_S)} \tag{43}$$

and use the representation (see equation (7.12.32) of [21])

$$P_\nu^m(\cos\vartheta) = \begin{cases} 0 & \text{if } \vartheta = 0 \\ \dfrac{(-1)^m 2\Gamma(\nu+m+1)}{\sqrt{\pi}\,\Gamma\left(m+\frac{1}{2}\right)\Gamma(\nu-m+1)} \dfrac{1}{(2\sin\vartheta)^m} \displaystyle\int_0^\vartheta \frac{\cos\left(\nu+\frac{1}{2}\right)t}{(2\cos t - 2\cos\vartheta)^{\frac{1}{2}-m}}\,\mathrm{d}t & \text{if } \vartheta \in (0,\pi) \end{cases} \tag{44}$$

to get rid of Euler's $\Gamma(\nu - m + 1)$ which is responsible for making $P_{n_0}^m$ vanish identically. In this way, the function $\varepsilon_\nu^m(\vartheta_c, \varrho)$ in $(42)_2$ is meaningful also when $\nu \to n_0$. Moreover, when $P_\nu^m(\cos\vartheta)$ in (44) is normalized to obey (26), $\Gamma(\nu - m + 1)$ disappears again and the second variation of $\mathcal{F}$ computed on $u_m(\vartheta, \varphi)$ converges to $\mu = n_0(n_0+1) - 2$ on the set of normalized Legendre functions. This procedure makes it also possible to treat the case $\nu = 0$.

It is easier to perform a stability analysis in the set $\mathcal{G} = \{(\vartheta_c, \varepsilon, \rho)\}$ by fixing ρ. In fact, we can easily solve (14) in terms of ε, treated as independent of ρ, arriving at

$$\varepsilon\left(\vartheta_c, \rho\middle|\vartheta_c^0\right) = \bar{\Theta}\left(\vartheta_c, \rho\middle|\vartheta_c^0\right) := \frac{\left(\cos\vartheta_c - \cos\vartheta_c^0\right)\sin\vartheta_c}{\rho\cos\vartheta_c - 1}. \tag{45}$$

By varying ϑ_c^0 in $[0, \pi]$ the graphs of $\varepsilon\left(\vartheta_c, \rho\middle|\vartheta_c^0\right)$ span the *admissible set* $\mathcal{A}$ (figure 7). The subset $\mathcal{A}_+ \subset \mathcal{A}$ where $\varepsilon > 0$ pertains to positive line tension, while the subset $\mathcal{A}_- \subset \mathcal{A}$ where $\varepsilon < 0$ pertains to negative line tension. Since the intersections between the graphs of $\varepsilon\left(\vartheta_c, \rho\middle|\vartheta_c^0\right)$ and $\varepsilon_*(\vartheta_c, \rho|\tau^*)$ in (17) cover the set $\mathcal{A}$ when ϑ_c^0 and τ^* are varied, any point in $\mathcal{A}$ is an equilibrium configuration corresponding to some point in $\mathcal{P}$. As to stability, we plot the graphs of the functions $\varepsilon_\nu^m(\vartheta_c, \rho)$ defined in (42). Then, we determine the values of ν for which the graphs of $\varepsilon_\nu^m(\vartheta_c, \rho)$ pass through a given point $P \in \mathcal{A}$: whenever P is on the graph of a function $\varepsilon_\nu^m(\vartheta_c, \rho)$ with $\nu \in \mathcal{U}$, the corresponding equilibrium configuration is unstable. Following the same avenue as in [12], we can check that any point in $\mathcal{A}$ lies on some curve $\varepsilon_\nu^m(\vartheta_c, \rho)$, for $\nu > 1$, and so stable modes always exist. When $m = 0$ the marginal curve $\varepsilon_1(\vartheta_c, \rho) := \varepsilon_1^0(\vartheta_c, \rho)$ divides $\mathcal{A}_+$ into two subsets: only the portion below $\varepsilon_1(\vartheta_c, \rho)$ is locally stable against modes with $m = 0$. When $m \geqslant 2$, the typical curve $\varepsilon_1^m(\vartheta_c, \rho)$ is plotted in figure 8: the points in $\mathcal{A}_-$ above the graph of $\varepsilon_1^m(\vartheta_c, \rho)$ are stable against modes labelled by m, while the points below it are unstable against the same modes. It is possible to check numerically that

$$\lim_{m\to\infty} \varepsilon_1^m(\vartheta_c, \rho) = 0$$

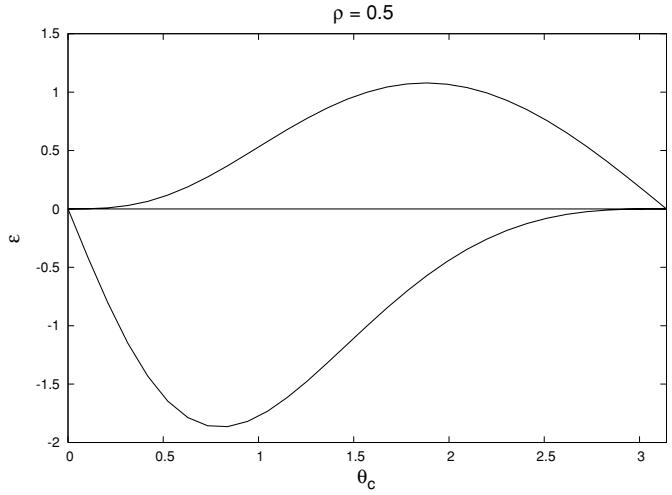

Figure 7. A cross section of the admissible set $\mathcal{A} \subset \mathcal{G}$ with the plane $\varrho = 0.5$. The region drawn here is bounded by the graphs of $\bar{\Theta}(\vartheta_c, 0.5|0)$ (upper curve) and $\bar{\Theta}(\vartheta_c, 0.5|\pi)$ (lower curve).

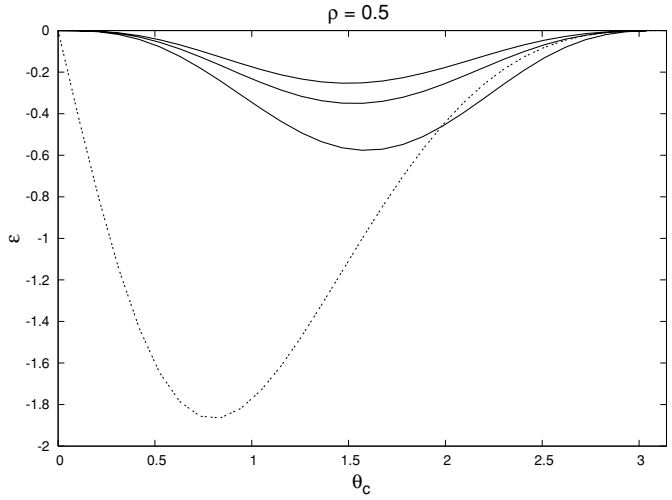

Figure 8. Cross sections of the surfaces $\varepsilon_1^m(\vartheta_c, \varrho)$ with the plane $\rho = 0.5$ of $\mathcal{G}$, for $m = 2, 3, 4$. On increasing m, $\varepsilon_1^m(\vartheta_c, 0.5)$ become closer and closer to the ϑ_c axis. Any surface $\varepsilon_1^m(\vartheta_c, \varrho)$ splits the subset $\mathcal{A}_-$ of the admissible set $\mathcal{A}$ into two subsets: only the subset above this surface is stable against modes labelled by m. The dashed line is the lower bound of the set $\mathcal{A}_-$.

so that the marginal curves tend to $\varepsilon = 0$ and the whole set $\mathcal{A}_-$ is unstable when m increases making the perturbed contour line wigglier and wigglier. This is consistent with the unboundedness from below of the functional $\mathcal{F}$ in (1) for negative line tensions. However, the length scale $\ell_m(\vartheta_c, \rho)$ of the oscillations induced by the destabilizing modes on $\mathcal{S}$ could be smaller than the typical length $\ell_c = |\xi|$ of the model. In that case, the modes would operate a length scale outside the range where the model based on (1) is acceptable and where other stabilizing effects, not accounted for in (1), are presumably at work. Thus, to be

consistent, the induced instability should not be accounted for in our model. One could be led by intuition to consider the wavelength of the corrugations induced on the contact line $\mathcal{C}$ as a good candidate for $\ell_m(\vartheta_c, \rho)$: on increasing m, the modes induce wigglier corrugations on $\mathcal{C}$. In fact, on dealing with sessile droplets sitting on flat substrates [12], a smaller length scale was revealed, which involves the oscillations induced by Legendre functions on the meridians of an unperturbed spherical droplet. Although the same avenue could be followed here, we prefer to measure the relative reliability of any reported negative value of τ by answering the following question: given ϑ_c^0, τ^* and ξ, how rich is the set of modes that do not destabilize a droplet? The property of unstable modes outlined before should convince that we need to control the highest value $m_{\rm rs}$ of m for which modes u_m are stable: we refer to this number as to the *index of residual stability* and we say that an equilibrium configuration is *residually stable* if $m_{\rm rs} > 2$. If $m_{\rm rs} = 2$ for some values of the constitutive parameters, unstable modes exist for all values of m, and the equilibrium configurations are simply unstable. The larger is $m_{\rm rs}$, the stronger is our expectation that the corresponding negative value of τ is reliable. In the next section we will see how $m_{\rm rs}$ is affected by the substrate's curvature.

4. Reverse mapping and bifurcation diagrams

The stability analysis of section 3 was performed in $\mathcal{G}$ where (32) was easier to solve. To explore stability in terms of the constitutive parameters we have to map the results into the space $\mathcal{P}$ and then take sections at fixed Ξ or Λ, according to the ensemble we study. At variance with [12], where we found an analytic map from the $(\vartheta_c, \varepsilon)$-plane into the $\left(\vartheta_c^0, \tau^*\right)$-plane, here a numerical strategy is more efficient since the presence of additional parameters makes the analytic avenue much more involved.

When the line tension is positive, two functions—$T_{\rm min}\left(\vartheta_c^0, \Xi\right)$ and $T_{\rm Max}\left(\vartheta_c^0, \Xi\right)$—can be defined (see appendix C), with the following property: one stable equilibrium and two unstable equilibria correspond to a given triple $\left(\vartheta_c^0, \tau^*, \Xi\right)$ if and only if

$$T_{\rm min}\left(\vartheta_c^0, \Xi\right) < \tau^* < T_{\rm Max}\left(\vartheta_c^0, \Xi\right). \tag{46}$$

When $\tau^* = T_{\rm min}\left(\vartheta_c^0, \Xi\right)$ or $\tau^* = T_{\rm Max}\left(\vartheta_c^0, \Xi\right)$, one marginally stable equilibrium and one unstable equilibrium exist for the triple $\left(\vartheta_c^0, \tau^*, \Xi\right)$. An important consequence of the definition of $T_{\rm min}\left(\vartheta_c^0, \Xi\right)$ and $T_{\rm Max}\left(\vartheta_c^0, \Xi\right)$ is that the equilibrium $p_2(\tau^*)$ is always stable, when it exists, while the equilibria $p_1(\tau^*)$ and $p_3(\tau^*)$ are unstable; for this reason, the regions in figures 3–5 where three equilibria exist are also the only regions where stable configurations exist (see appendix D).

When the line tension is negative, we already know from section 3 that destabilizing modes exist for the equilibrium configuration corresponding to a given triple $P \equiv \left(\vartheta_c^0, \tau^*, \Xi\right)$. We can define a function $T^m_{\rm Max}\left(\vartheta_c^0, \Xi\right)$ with the following property: the equilibrium at given ϑ_c^0 and Ξ is stable against modes u_{m^*} with m^* ranging from 2 to m if and only if

$$|\tau^*| < T^m_{\rm Max}\left(\vartheta_c^0, \Xi\right).$$

When $\Xi \to 0$, and so the substrate tend to be flat, we recover the results of [12]. For a given $\Xi < 0$, the function $T^m_{\rm Max}\left(\vartheta_c^0, \Xi\right)$ with $m > 2$ is defined in the interval $\left(\bar{\vartheta_c}^1(\Xi, m), \bar{\vartheta_c}^2(\Xi, m)\right)$ and diverges when ϑ_c^0 tends to either $\bar{\vartheta_c}^1(\Xi, m)$ or $\bar{\vartheta_c}^2(\Xi, m)$. If either $\vartheta_c^0 < \bar{\vartheta_c}^1(\Xi, m)$ or $\vartheta_c^0 > \bar{\vartheta_c}^2(\Xi, m)$, the corresponding equilibrium configurations are unstable, regardless of the value of $|\tau^*|$. At variance with the case $\Xi = 0$ where $\bar{\vartheta_c}^1(0, m) = 0$ and $\bar{\vartheta_c}^2(0, m) = \pi$ for any $m > 2$, when $\Xi < 0$ the interval $\left(\bar{\vartheta_c}^1(\Xi, m), \bar{\vartheta_c}^2(\Xi, m)\right)$ shrinks on increasing m and vanishes when m attains a critical value $\overline{m}$. While we refer the interested reader to appendix E for a detailed discussion, here we just draw an important conclusion from this result: for

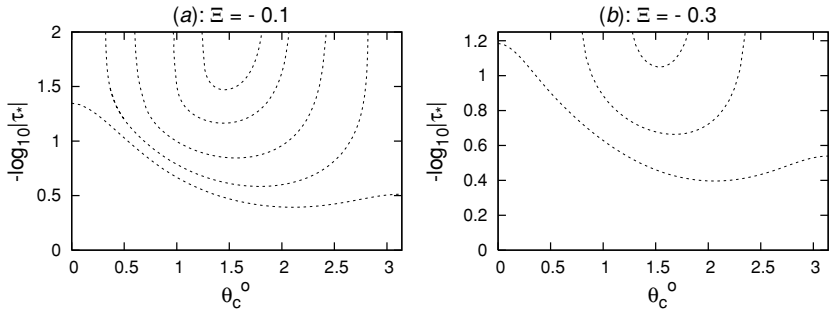

Figure 9. Graphs of $\log_{10}|T^m_{\mathrm{Max}}(\vartheta^0_c, \Xi)|$ at fixed values of Ξ. On the left, where $\Xi = -0.1$, $\log_{10}|T^m_{\mathrm{Max}}(\vartheta^0_c, 0.1)|$ has been plotted for $m = 2, 3, 5, 8, 10$. On the right, where $\Xi = -0.3$, we plotted $\log_{10}|T^m_{\mathrm{Max}}(\vartheta^0_c, 0.3)|$ for $m = 2, 3, 4$. When m increases, the domain of the function $T^m_{\mathrm{Max}}(\vartheta^0_c, \Xi)$ shrinks.

any fixed $\Xi < 0$, there exists a value $\bar{m} < +\infty$ such that any equilibrium configuration with negative line tension is made unstable by modes u_m with $m \geqslant \bar{m}$. For instance, when $\Xi = 0.012, 0.1, 0.3, 0.35, 0.5$, the values of $\bar{m}$ are $\bar{m} = 81, 11, 5, 4, 3$, respectively (figure 9). As a consequence, the index of residual stability $m_{\mathrm{rs}} < \bar{m}$ is equal to 2 for any equilibrium configuration when the radius of the substrate becomes comparable with ξ, as in the case of colloidal particles. In [12] we showed that for most of the experimental values in [19] reporting a negative line tension, the index of residual stability was close to 50. Without changing the values of the line and the surface tensions, the bare contact angle and the volume of the droplet studied in [19], we conclude that the substrate's curvature has a destabilizing role, since $\bar{m}$ falls below 50 when Ξ varies from 0.01 to 0.1. This result is important for applications in colloid science since it proves that a negative line tension is unlikely to stabilize emulsions, especially when the solid particles are very small. We stress that this result can be arrived at only by a local stability analysis and not by means of a comparison between energies as made in [5].

Figure 10(*b*)–(*d*) shows the bifurcation diagrams at $|\Xi| = 0.3$. When $\vartheta^0_c < \vartheta^0_{cm}$ (figure 10(*b*)), a stable equilibrium configuration exists provided the droplet's volume neither exceeds an upper bound, nor lies below a lower bound. When $\vartheta^0_{cm} < \vartheta^0_c < \vartheta^0_{cM}$ (figure 10(*c*)) a stable equilibrium exists provided that the volume of the droplet is large enough. Finally, if $\vartheta^0_c > \vartheta^0_{cM}$ (figure 10(*d*)), no stable equilibrium exists. At this level, where the line tension has been prescribed, each bifurcation diagram contained in figure 10 is indeed the juxtaposition of two separate diagrams, one for positive and one for negative line tension. It is worth noting that on passing from positive to negative line tension the equilibrium contact angle suffers a jump that vanishes when $\Xi \to 0$.

The destabilizing effect of the substrate's curvature is also shown in figure 2 from which is clear that, for a given positive line tension and a given droplet's volume, increasing Ξ makes the region where three equilibria exist smaller: since we now know that this is the only region where a stable equilibrium exists, the result immediately follows.

To study the effects of line tension on stability, we map our results in the Λ-ensemble. Figure 11 refers to $\vartheta^0_c = 7\pi/16$ and $\vartheta^0_c = 9\pi/16$, while $\Lambda = 100$ in both cases. The stable branches always correspond to the equilibrium $p_2(\tau^*)$ which connects to either $p_3(\tau^*)$ or $p_1(\tau^*)$, depending on the value of ϑ^0_c. Thus, in this case, the results parallel those obtained for flat substrates: when the line tension is positive a stable equilibrium exists provided that the line tension lies below a critical value. Figure 12 parallels figure 6 and shows how a

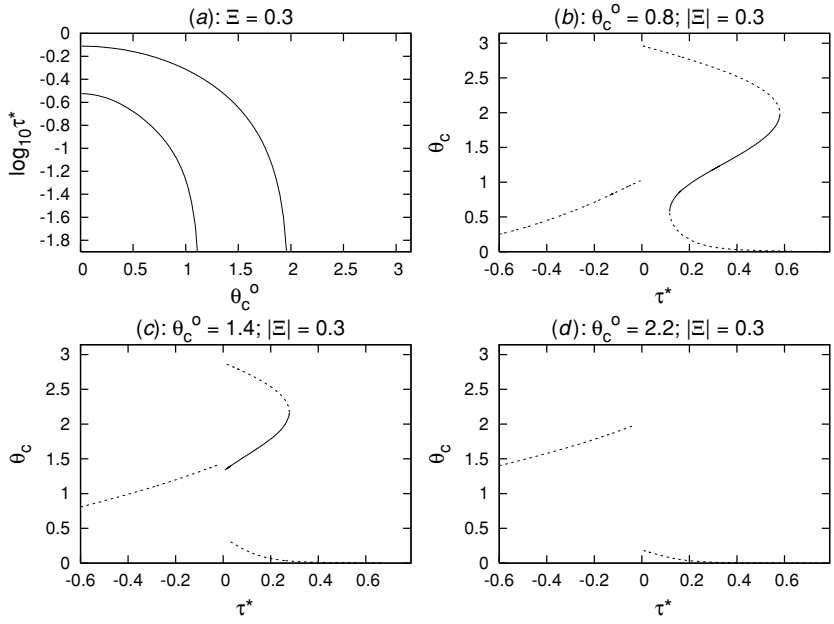

Figure 10. Bifurcation diagrams at $|\Xi| = 0.3$, for different values of ϑ_c^0. We start discussing the case where line tension is positive. In (a) we reproduced the part of figure 3 corresponding to $\Xi = 0.3$, from which it is possible to see how the number of equilibria varies with τ^*, according to the value of ϑ_c^0. $(b)\vartheta_c^0 = 0.8 < \vartheta_{cm}^0$. The locally stable equilibrium $p_2(\tau^*)$ exists when τ^* ranges in $[\tau^*_{\min}(\vartheta_c^0, \Xi), \tau^*_{\mathrm{Max}}(\vartheta_c^0, \Xi)]$, but it is not globally stable (see section 5). Outside this range, there are no stable equilibria. $(c)\vartheta_{cm}^0 < \vartheta_c^0 = 1.4 < \vartheta_{cM}^0$. The locally stable equilibrium $p_2(\tau^*)$ exists in the range $\tau^* \in [0, \tau^*_{\mathrm{Max}}(\vartheta_c^0, \Xi)]$, but it is not globally stable (see section 5). $(d)\vartheta_c^0 = 2.2 > \vartheta_{cM}^0$. Only the unstable equilibrium $p_1(\tau^*)$ exists. When $\tau^* < 0$, a unique equilibrium exists which is conditionally stable.

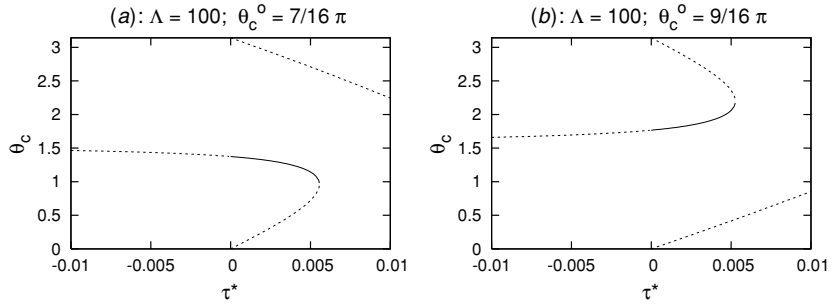

Figure 11. Bifurcation diagrams at $\Lambda = 100$ and $\vartheta_c^0 = 7\pi/16(a)$, $\vartheta_c^0 = 9\pi/16(b)$. When $\tau^* < 0$, a unique equilibrium exists which is unstable against modes with large enough m. When $\tau^* > 0$ the solution survives as the branch $p_2(\tau^*)$, which is locally, but not globally stable until it merges at a turning point with an unstable branch: $p_1(\tau^*)$ in (a), $p_3(\tau^*)$ in (b). An isolated branch exists for any positive τ^*, but it is always unstable.

bifurcation diagram like that in figure 11(a) transforms into a diagram like that in figure 11(b) on decreasing Λ. We first note that, since Λ is fixed and we consider only values $\Xi < 1$, τ^* should have an upper bound by (13). In figure 12 we consider the cases where

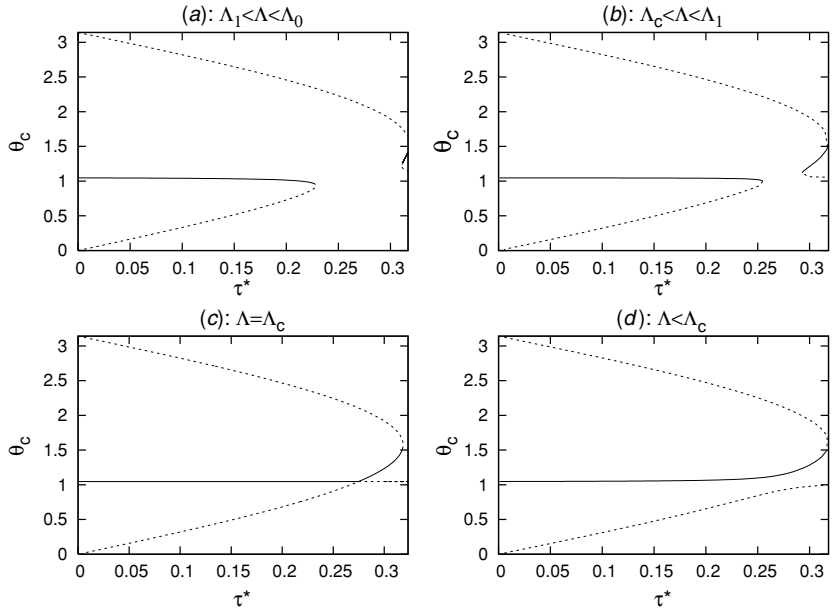

Figure 12. Bifurcation diagrams at $\vartheta_c^0 = \pi/3$ and $\Lambda = 3.155(a), 3.105(b), 3.09296(c)$, and $3.05(d)$. This diagram shows how a bifurcation diagram like that in figure 11(a) changes in a bifurcation diagram like that in figure 11(b), when $\vartheta_c^0 < \pi/2$ and Λ is sufficiently small. In fact the bifurcation diagrams parallel the results introduced in figure 6. When the locally stable equilibrium p_2 exists, it is not globally stable (see section 5).

$\Lambda \in [\Lambda_1, \Lambda_0], \Lambda \in [\Lambda_c, \Lambda_1], \Lambda = \Lambda_c$ and $\Lambda < \Lambda_c$, respectively; below $\Lambda = \Lambda_c$, we recover a diagram like that of figure 11(b).

5. First-order transitions

As mentioned in the introduction, first-order transitions escape the local stability analysis outlined in sections 3 and 4. To complete our study we need to compare the energy of a droplet laid on a substrate with that of a droplet detached from a substrate and, possibly, with that of a droplet surrounding a substrate. This latter case is important when $R \ll r$, as frequently occurs when colloidal particles are dispersed in an emulsion. We rephrase our notation into that employed in [5] (see table 1). To draw a meaningful comparison, we note that the energy G of the particle *and* the adhering droplet is

$$G[\mathcal{B}] := \mathcal{F}[\mathcal{B}] + 4\pi\gamma_{sc}R^2,$$

where the last term is introduced to account for the total energy penalty associated with the solid-continuous phase interface. Clearly, the last term is a constant that does not affect the local analysis performed before, but it should be introduced here where $G(\mathcal{B})$ has to be compared with either the energy G_d of a spherical droplet, detached from the substrate, of radius

$$r_d := \sqrt[3]{\frac{3V}{4\pi}}$$

or with the energy G_e of a spherical droplet of radius

$$r_e := \sqrt[3]{\frac{3V}{4\pi} - R^3}$$

which encapsulates the substrate of radius R. Both r_d and r_e are chosen so as to enforce the incompressibility constraint. In the former case

$$G_d = 4\pi r_d^2 \gamma_{\mathrm{ow}} + 4\pi R^2 \gamma_{\mathrm{sc}},$$

while in the latter

$$G_e = 4\pi r_e^2 \gamma_{\mathrm{ow}} + 4\pi R^2 \gamma_{\mathrm{sd}}.$$

By comparing G_d with G_e, we can easily conclude that

$$\frac{G_d - G_e}{\sqrt[3]{\left(\frac{3V}{4\pi}\right)}} = \left(1 - \sqrt[3]{1 - \frac{V_s}{V}}\right)\left(1 + \sqrt[3]{1 - \frac{V_s}{V}}\right) + \cos\vartheta_c^0 \sqrt[3]{\left(\frac{V_s}{V}\right)^2}, \tag{47}$$

where $V_s := \frac{4\pi R^3}{3}$ is the volume of the substrate. Since, by (13), $V_s/V = 4/\Lambda^3$ we also have

$$\frac{G_d - G_e}{\sqrt[3]{\left(\frac{3V}{4\pi}\right)}} = \left(1 - \sqrt[3]{\left(1 - \frac{4}{\Lambda^3}\right)^2}\right) + \cos\vartheta_c^0 \sqrt[3]{\left(\frac{4}{\Lambda^2}\right)^2} \tag{48}$$

from which we see that encapsulation is preferred to detachment whenever

$$\cos\vartheta_c^0 > \cos\vartheta_c^{0*} =: \left(\sqrt[3]{\left(1 - \frac{4}{\Lambda^3}\right)^2} - 1\right)\left(\sqrt[3]{\left(\frac{4}{\Lambda^2}\right)^2}\right)^{-1}. \tag{49}$$

In the limit where $V \gg V_s$, $\cos\vartheta_c^{0*} \approx -\frac{2}{3}\left(\frac{V_s}{V}\right)^{1/3}$, and so ϑ_c^{0*} approaches $\pi/2$. Equation (48) also shows that $G_d - G_e > 0$, and so encapsulation is preferred to detachment, whenever $\vartheta_c^0 < \pi/2$ and $\Lambda > \sqrt[3]{2}$.

After some algebraic manipulations, we arrive at

$$G[\mathcal{B}] = 2\pi r^2 \gamma_{\mathrm{ow}}(1 - \cos\vartheta_{\mathcal{S}}) + 2\pi R^2 \gamma_{\mathrm{sc}}\left(1 + \cos\vartheta_{\mathcal{S}_*}\right) + 2\pi\gamma_{\mathrm{sd}} R^2\left(1 - \cos\vartheta_{\mathcal{S}_*}\right) + 2\pi\tau R \sin\vartheta_{\mathcal{S}_*}$$

which should be compared with G_e if (47) holds, and with G_d otherwise. By rescaling the energies to $\gamma_{\mathrm{ow}}\left(\frac{3V}{\pi}\right)^{2/3}$ [22] and recalling the definitions of ϑ_c^0 (3), Λ (13), τ^* (12), and ϱ (5) we finally need to ascertain the sign of either

$$G[\mathcal{B}] - G_e = 2\pi\left[\left(\frac{\varrho}{\Lambda}\right)^2(1 - \cos\vartheta_{\mathcal{S}}) - 2\sqrt[3]{\left(\frac{1}{4} - \frac{1}{\Lambda^3}\right)^2}\right] + \frac{2\pi}{\Lambda^2}\cos\vartheta_c^0\left(1 + \cos\vartheta_{\mathcal{S}_*}\right) + \frac{2\pi}{\Lambda}\tau^* \sin\vartheta_{\mathcal{S}_*}, \tag{50}$$

if (49) hold

$$G[\mathcal{B}] - G_d = 2\pi\left[\left(\frac{\varrho}{\Lambda}\right)^2(1 - \cos\vartheta_{\mathcal{S}}) - \frac{1}{\sqrt[3]{2}}\right] - \frac{2\pi}{\Lambda^2}\cos\vartheta_c^0(1 - \cos\vartheta_{\mathcal{S}_*}) + \frac{2\pi}{\Lambda}\tau^* \sin\vartheta_{\mathcal{S}_*} \tag{51}$$

otherwise.

A complete study of equations (50)–(51) is beyond the scopes of the present paper. We checked the sign of the energy differences in equations (50)–(51) in several cases. For the parameters chosen in figures 10–12, the locally stable branch p_2 is never globally stable. In

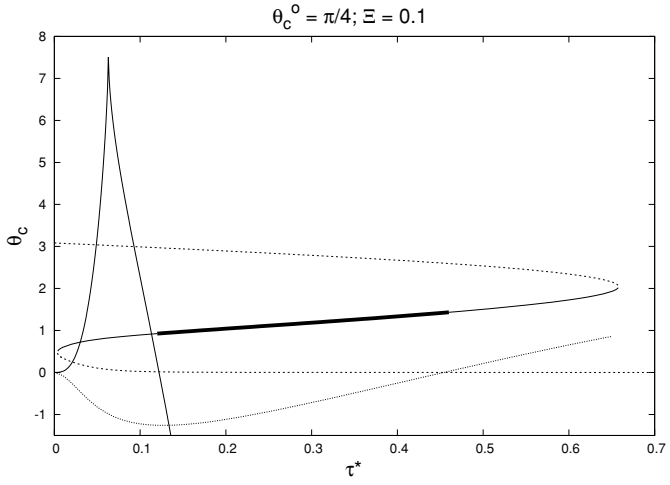

Figure 13. A bifurcation diagram at $\Xi = 0.1$ and $\vartheta_c^0 = \pi/4$ is plotted together with the graphs of (50) (solid line) and (51) (dotted line). The locally stable equilibrium $p_2(\vartheta_c)$ is also globally stable when $\tau^* \in (0.12, 0.46)$—thick, solid segment on the bifurcation diagram—where both (50) and (51) are negative. Outside this set, either encapsulation ($\tau^* < 0.12$) or detachment ($\tau^* > 0.46$) are energetically favoured.

the Λ-ensemble (figures 11–12), it is easy to determine from (48) if either encapsulation or detachment is favoured, while this comparison is harder in the Ξ-ensemble. As a result, encapsulation is preferred in the cases illustrated in figures 11(a) and 12, whereas detachment is preferred in the case shown in figure 11(b). On the other hand, figure 13 shows a case where, for given values of Ξ and ϑ_c^0, the branch p_2 is also globally stable when τ^* ranges in a suitable interval. Encapsulation is preferred when τ^* is small enough—and so the droplet's volume is large— while detachment is preferred if τ^* is large enough. This latter transition is the analogue of the drying transition found by Widom [22] on a flat substrate, whereas the transition to encapsulation is induced by the substrate's curvature. Although we have no elements to state a general rule, there are indications that the substrate's curvature hampers the global stability of equilibria with the droplet sitting on the substrate.

6. Conclusions

The stability of sessile droplets laid upon a spherical substrate was studied by applying a general stability criterion. As in the case where the substrate is flat, different behaviours exist according to the sign of line tension. Here, however, there is a complex interplay between the bare contact angle and the typical length scales of the problem that makes the results of the stability analysis rather interesting also for positive line tensions. In particular, we singled out regimes where the presence of a curved substrate prevents the existence of locally stable sessile droplets. In this case, the droplet can either detach itself from the substrate or can wrap around the substrate, if this latter is sufficiently small, depending on the bare contact angle. The substrate's curvature enhances the destabilizing role of negative line tensions by drastically reducing the index of residual instability as compared to the case where the substrate is flat. This leads us to a critical reconsideration of claims concerning the stabilizing role played by negative line tension on emulsions that were based only upon energy comparisons. Finally,

we also performed a global stability analysis in several cases that indicate how the substrate's curvature hampers the global stability of sessile droplets.

The results of this paper call for different extensions. First, the lack of stability for positive line tension demands a deepen study that will be presented elsewhere [23]. In particular, it would be interesting to optimize the range in the Λ-ensemble where no stable equilibria exist, by looking at its dependence on the bare contact angle. Extensions to other geometries that were preliminary studied in [24] could also be pursued, as well as a complete treatment of global stability. It would also be interesting to apply the techniques employed here to assess the local stability of acicular particles at an interface between two liquids, to complete the global stability analysis performed in [25]. Finally, a systematic study of curvature corrections in the free-energy functional (1) will help in clarifying the destabilizing role played by line tension [15].

Acknowledgment

We acknowledge Professor Epifanio G Virga for useful discussions.

Appendix A. The functions $\tau_c^{*M}\left(\vartheta_c^0, \Xi\right)$ and $\tau_c^{*m}\left(\vartheta_c^0, \Xi\right)$

The function $\Upsilon\left(\vartheta_c \middle| \vartheta_c^0, \tau^*, \Xi\right)$ defined in (19) attains a local maximum $\Upsilon^M\left(\tau^* \middle| \vartheta_c^0, \Xi\right)$ at $\vartheta_c =: \vartheta_{c\Upsilon}^M$ which is determined by use of Netwon's method (see, e.g., [26]) which does not involve the derivative of $\Upsilon\left(\vartheta_c \middle| \vartheta_c^0, \tau^*, \Xi\right)$. For a given pair $\left(\vartheta_c^0, \Xi\right)$, the function $\Upsilon^M(\tau^*)$ is strictly decreasing and hence it vanishes at one point $\tau_c^{*M}\left(\vartheta_c^0, \Xi\right)$, at most. Moreover, since $|\tau^*| < 1$, by (23) $\tau_c^{*M}\left(\vartheta_c^0, \Xi\right)$ exists if and only if

$$\Upsilon^M(1) < 0 \cap \Theta^M\left(\vartheta_c^0, \Xi\right) > 0.$$

To compute $\tau_c^{*M}\left(\vartheta_c^0, \Xi\right)$, we first determine $\Upsilon^M\left(\tau^* \middle| \vartheta_c^0, \Xi\right)$ by resorting to approximation methods, and then we note that $\Upsilon^M(1|\vartheta_c^0, \Xi) < 0$ while $\Upsilon^M(10^{-i}|\vartheta_c^0, \Xi) > 0$ for an integer $i > 0$. Since $\tau_c^{*M}\left(\vartheta_c^0, \Xi\right)$ is the zero of $\Upsilon^M\left(\tau^* \middle| \vartheta_c^0, \Xi\right)$, applying the bisection method to $\Upsilon^M\left(\tau^* \middle| \vartheta_c^0, \Xi\right)$ yields $\tau_c^{*M}\left(\vartheta_c^0, \Xi\right)$. A similar avenue is followed to define and approximate $\tau_c^{*m}\left(\vartheta_c^0, \Xi\right)$.

Appendix B. The critical value $\Lambda_c\left(\vartheta_c^0\right)$

We determine a sequence $\{\Lambda_n\}$ that converges to the critical value $\Lambda_c\left(\vartheta_c^0\right)$ of Λ defined in section 2. We first recall that if $\Lambda_c < \Lambda_n < 1/\tau_c^{*m}$, the Λ_n-curve intersects the curve τ_c^{*M} at $\Xi = \Xi^1_{\Lambda_n}$ and at $\Xi = \Xi^2_{\Lambda_n} > \Xi^1_{\Lambda_n}$. We also note that if $\Lambda_c < \Lambda_1 < \Lambda_2 < 1/\tau_c^{*m}$ the Λ_1-curve and the Λ_2-curve do not intersect each other because of their convexity and that the following relation holds:

$$\Xi^1_{\Lambda_1} < \Xi^1_{\Lambda_2} < \Xi^2_{\Lambda_2} < \Xi^2_{\Lambda_1}. \tag{B.1}$$

We define the sequence $\{\Lambda_n\}$ by use of the following recursive procedure.

- Given Λ_n and the points $\Xi^1_{\Lambda_n}, \Xi^2_{\Lambda_n}$, we select $\Xi_{\Lambda_{n+1}} \in \left(\Xi^1_{\Lambda_n}, \Xi^1_{\Lambda_n}\right)$. To improve the convergence rate of the sequence $\{\Lambda_n\}$, $\Xi_{\Lambda_{n+1}}$ is taken as the abscissa of the intersection between the tangent lines to the Λ_n-curve at the points $\Xi^1_{\Lambda_n}$ and $\Xi^2_{\Lambda_n}$.
- From (13), we determine the unique value Λ_{n+1} of Λ such that the Λ_{n+1}-curve passes through the point $\Xi_{\Lambda_{n+1}}$.
- We ascertain if $\Xi_{\Lambda_{n+1}}$ is the smallest or the largest intersection between the Λ_{n+1}-curve and τ_c^{*M} by evaluating the difference between these functions when $\Xi \simeq \Xi_{\Lambda_{n+1}}$.

- We compute the other intersection between the Λ_{n+1}-curve and τ_c^{*M} by the bisection method.

The sequence $\{\Lambda_n\}$ converges to Λ_c since

$$\lim_{n\to\infty}\left(\Xi^2_{\Lambda_n}-\Xi^1_{\Lambda_n}\right)=0, \tag{B.2}$$

as can be proved by use of (B.1).

Appendix C. The functions $T_{\min}(\vartheta_c^0,\Xi), T_{\mathrm{Max}}(\vartheta_c^0,\Xi)$ and $T^m_{\mathrm{Max}}(\vartheta_c^0,\Xi)$

In section 3 we introduced the marginal curves defined through (42). There, we worked at fixed values of ρ, to use planar sets of $\mathcal{G}$. To rephrase the stability analysis in the space $\mathcal{P}$ we need to study the marginal curves with fixed parameters ϑ_c^0 and Ξ. Since ρ is given by (18) on an equilibrium configuration, we can define the function

$$S^m\left(\vartheta_c|\vartheta_c^0,\Xi\right):=\varepsilon_1^m\left(\vartheta_c,f\left(\vartheta_c|\vartheta_c^0,\Xi\right)\right). \tag{C.1}$$

Let us first focus on positive line tensions. Since ε obeys (15) and, for any fixed ρ, the region in $\mathcal{A}_+$ below $\varepsilon_1^0(\vartheta_c,\rho)$ is stable, we can define the *stable interval* as the subset of $\mathcal{A}_+$ where, for any given pair $\left(\vartheta_c^0,\Xi\right)$, the inequality

$$S\left(\vartheta_c|\vartheta_c^0,\Xi\right):=S^0\left(\vartheta_c|\vartheta_c^0,\Xi\right)\geqslant\Theta\left(\vartheta_c|\vartheta_c^0,\Xi\right) \tag{C.2}$$

holds. Only points in $\mathcal{G}$ satisfying inequality (C.2) are stable and hence, to determine the stability of equilibria in $\mathcal{P}$, we find the values of $\tau^*\geqslant 0$ for which one root of (19) belongs to the stable interval. Let $T_{\min}\left(\vartheta_c^0,\Xi\right)$ and $T_{\mathrm{Max}}\left(\vartheta_c^0,\Xi\right)$ be the values of τ^* such that a zero of (19) is either at the left- or at the right-end of the stable interval. Hence, a given triple $\left(\vartheta_c^0,\tau^*,\Xi\right)$ has one stable equilibrium if inequality (46) holds. To arrive at $T_{\min}\left(\vartheta_c^0,\Xi\right)$ and $T_{\mathrm{Max}}\left(\vartheta_c^0,\Xi\right)$, we first determine the left- and the right-end points of the stable interval by solving the equation

$$\Theta\left(\vartheta_c|\vartheta_c^0,\Xi\right)=S^0\left(\vartheta_c|\vartheta_c^0,\Xi\right)>0. \tag{C.3}$$

In solving $(\mathrm{C.3})_1$ we disregard the spurious solutions with $\Theta\left(\vartheta_c|\vartheta_c^0,\Xi\right)=0$ that always exist. In fact, as explained in section 2, when $\Theta\left(\vartheta_c|\vartheta_c^0,\Xi\right)\to 0$, $f\left(\vartheta_c|\vartheta_c^0,\Xi\right)$ diverges and so, by equations (11), (15) and (18) both ε_m^0 and $S^0\left(\vartheta_c|\vartheta_c^0,\Xi\right)$ tend to zero. However, we also remarked in section 2 that $\varepsilon=0$ is an acceptable equilibrium solution only when line tension vanishes. Hence, when the left-end point of the stable interval satisfies $\Theta\left(\vartheta_c|\vartheta_c^0,\Xi\right)=0$, only the function $T_{\mathrm{Max}}\left(\vartheta_c^0,\Xi\right)$ is defined and we can set $T_{\min}\left(\vartheta_c^0,\Xi\right)\equiv 0$.

Solving $(\mathrm{C.3})_1$ is a non-trivial task since we do not know *a priori* how many roots it has. To overcome this difficulty, after approximating the functions $S^0\left(\vartheta_c|\vartheta_c^0,\Xi\right)$ and $\Theta\left(\vartheta_c|\vartheta_c^0,\Xi\right)$ by means of polynomials, we resorted to *simultaneous zero-finding algorithms* (see, e.g., [27] and [28]).

The second step is the evaluation of the functions $T_{\mathrm{Max}}\left(\vartheta_c^0,\Xi\right)$ and $T_{\min}\left(\vartheta_c^0,\Xi\right)$. Let the stable interval lie between $\vartheta_c^0=\vartheta_c^1$ and $\vartheta_c^0=\vartheta_c^2>\vartheta_c^1$. The function $T_{\min}\left(\vartheta_c^0,\Xi\right)$ is defined as the zero of the equation

$$\Upsilon\left(\vartheta_c^1|\vartheta_c^0,T_{\min}\left(\vartheta_c^0,\Xi\right),\Xi\right)=0, \tag{C.4}$$

and it is well defined because $\Upsilon\left(\vartheta_c|\vartheta_c^0,\tau^*,\Xi\right)$ is a strictly decreasing function of τ^* and $\Theta\left(\vartheta_c^1|\vartheta_c^0,\Xi\right)>0$. Similarly, the function $T_{\mathrm{Max}}\left(\vartheta_c^0,\Xi\right)$ is defined as the zero of the

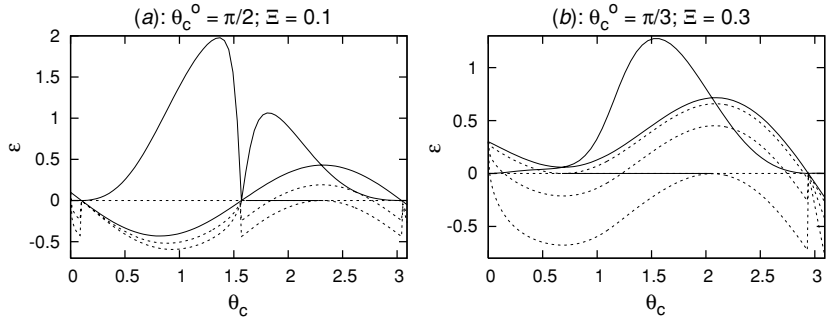

Figure 14. Graphs of several functions have been plotted in the $(\vartheta_c, \varepsilon)$-plane, for $(\vartheta_c^0, \Xi) = (\frac{\pi}{2}, 0.1)(a)$ and $(\frac{\pi}{3}, 0.3)(b)$. In (a) the solid lines represent $S(\vartheta_c|\frac{\pi}{2}, 0.1)$—the graph with a cusp—and $\Theta(\vartheta_c|\frac{\pi}{2}, 0.1)$. Dashed lines represent $\Upsilon(\vartheta_c|\frac{\pi}{2}, 0.1529, 0.1)$ and $\Upsilon(\vartheta_c|\frac{\pi}{2}, 0.2751, 0.1)$. The stable interval is the solid segment $[1.5708, 2.30465]$ bounded by the values of ϑ_c where $\Theta(\vartheta_c|\frac{\pi}{2}, 0.1)$ and $\Upsilon(\vartheta_c|\frac{\pi}{2}, 0.2751, 0.1)$ intersect the ϑ_c axis. In this case, the root $p_2(\tau^*)$ of equations (15) and (19) corresponds to a stable equilibrium configuration when $\tau^* \leqslant T^*_{\mathrm{Max}}(\vartheta_c^0, \Xi) = \tau_c^M(\vartheta_c^0, \Xi)$. In (b) the solid lines represent $S(\vartheta_c|\frac{\pi}{3}, 0.3)$ (upper curve) and $\Theta(\vartheta_c|\frac{\pi}{3}, 0.3)$, while the dashed lines are $\Upsilon(\vartheta_c|\frac{\pi}{3}, 0.001, 0.3)$, $\Upsilon(\vartheta_c|\frac{\pi}{3}, 1.2510^{-7}, 0.3)$ and $\Upsilon(\vartheta_c|\frac{\pi}{3}, 1.3220210^{-13}, 0.3)$. The stable interval is now the solid segment $[0.6911, 2.0483]$ bounded by the intersections of $\Upsilon(\vartheta_c|\frac{\pi}{3}, 1.3220210^{-13}, 0.3)$ and $\Upsilon(\vartheta_c|\frac{\pi}{3}, 0.001, 0.3)$ with the ϑ_c-axis.

equation:

$$\Upsilon\big(\vartheta_c^2\big|\vartheta_c^0, T_{\mathrm{Max}}\big(\vartheta_c^0, \Xi\big), \Xi\big) = 0. \tag{C.5}$$

To evaluate $T_{\mathrm{min}}\big(\vartheta_c^0, \Xi\big)$ and $T_{\mathrm{Max}}\big(\vartheta_c^0, \Xi\big)$, we only need to apply the bisection method to equations (C.4)–(C.5), using the values of ϑ_c^1 and ϑ_c^2 obtained at the first step.

We conclude by sketching the definition of $T^m_{\mathrm{Max}}\big(\vartheta_c^0, \Xi\big)$, required when $\tau^* < 0$. The *m-stable interval* is defined as the subset of $\mathcal{A}_-$ where

$$S^m\big(\vartheta_c\big|\vartheta_c^0, \Xi\big) \leqslant \Theta\big(\vartheta_c\big|\vartheta_c^0, \Xi\big) \qquad \text{with} \quad m \geqslant 2. \tag{C.6}$$

As before, the end-points of the m-stable interval satisfy the equation

$$\Theta\big(\vartheta_c\big|\vartheta_c^0, \Xi\big) = S^m\big(\vartheta_c\big|\vartheta_c^0, \Xi\big) < 0 \tag{C.7}$$

which possesses at most one solution ϑ_c^2 that, in turn, is smaller than the unique zero $\bar{\vartheta}_c{}^{(1)}$ of $\Theta\big(\vartheta_c\big|\vartheta_c^0, \Xi\big)$ when the line tension is negative. Since $\Theta\big(\vartheta_c\big|\vartheta_c^0, \Xi\big)$ is negative if and only if $\vartheta_c < \bar{\vartheta}_c{}^{(1)}$, and $S^m\big(\vartheta_c\big|\vartheta_c^0, \Xi\big)$ is non positive, we conclude that the m-stable interval is $\big[\vartheta_c^2, \bar{\vartheta}_c{}^{(1)}\big]$ and so it has the spurious solution to (C.7) as its right-end point.

Appendix D. Stability of the equilibrium configuration $p_2(\tau^*)$

A numerical computation shows that the functions $T_{\mathrm{min}}\big(\vartheta_c^0, \Xi\big)$ and $T_{\mathrm{Max}}\big(\vartheta_c^0, \Xi\big)$ coincide, respectively, with the functions $\tau_c^{*m}\big(\vartheta_c^0, \Xi\big)$ and $\tau_c^{*M}\big(\vartheta_c^0, \Xi\big)$ defined in section 2. Hence the equilibria p_2 and p_3 coalesce precisely at the right-end point of the stable interval while coalescence of p_1 and p_2 occurs at the left-end point of the stable interval: the marginal curve passes through the points where the number of solutions varies from three to one and a turning point is expected in the bifurcation diagrams. Whenever the left end-point of a stable interval is also a root of (15) (see figure 14) we conclude that there exists a critical value $T_{\mathrm{Max}}\big(\vartheta_c^0, \Xi\big)$ such

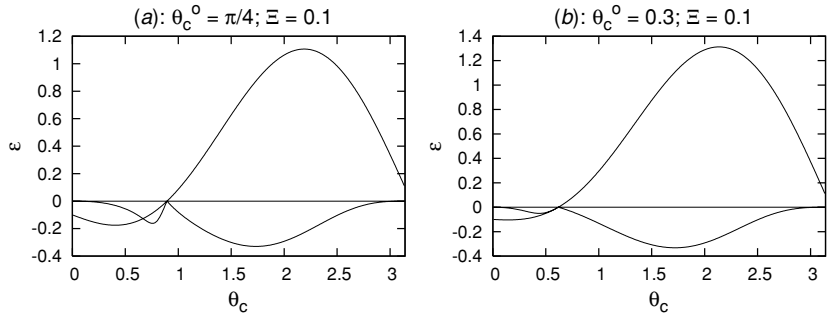

Figure 15. The functions $\Theta(\vartheta_c|\vartheta_c^0, \Xi)$ and $S^m(\vartheta_c|\vartheta_c^0, \Xi)$ for $\Xi = 0.1, m = 3$ and $\vartheta_c^0 = \pi/4$ and $\vartheta_c^0 = 0.3 \equiv \vartheta_c^{ms}(0.1, 3)$ have been plotted here. On moving ϑ_c^0 towards the value $\vartheta_c^0 = 0.3$ the 3-stable interval shrinks. At $\vartheta_c^0 = 0.3$, the functions $\Theta(\vartheta_c|\vartheta_c^0, \Xi)$ and $S^m(\vartheta_c|\vartheta_c^0, \Xi)$ have the same tangent line.

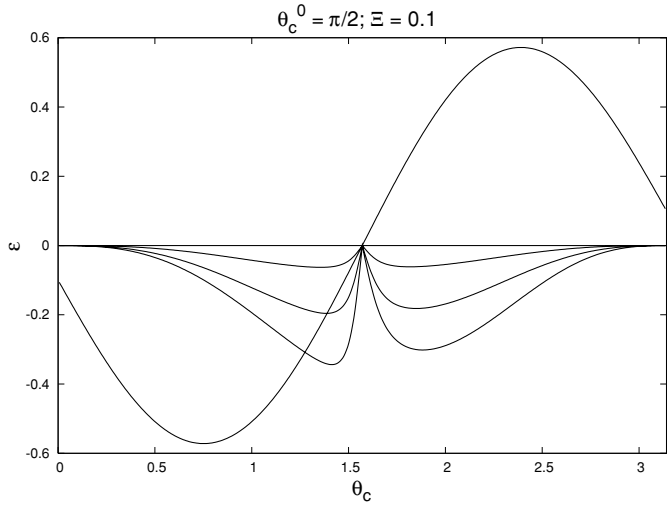

Figure 16. The function $\Theta(\vartheta_c|\vartheta_c^0, \Xi)$ for $\vartheta_c^0 = \pi/2$ has been plotted together with the functions $S^m(\vartheta_c|\vartheta_c^0, \Xi)$ for $\Xi = 0.1$, and $m = 3, 5, 15$. The curves $S^3(\vartheta_c|\vartheta_c^0, \Xi)$ and $S^5(\vartheta_c|\vartheta_c^0, \Xi)$ intersect $\Theta(\vartheta_c|\vartheta_c^0, \Xi)$ twice. The smallest intersection determines ϑ_c^2 whereas the larger is always the unique root of $\Theta(\vartheta_c|\vartheta_c^0, \Xi)$. When $m \geqslant 15$ only this latter intersection $\Theta(\vartheta_c|\vartheta_c^0, \Xi)$ and $S^m(\vartheta_c|\vartheta_c^0, \Xi)$ survives and so the function $T^m_{\mathrm{Max}}(\vartheta_c^0, \Xi)$ cannot be defined.

that the root $p_2(\tau^*)$ is stable for $\tau^* \in \left[0, T_{\mathrm{Max}}\left(\vartheta_c^0, \Xi\right)\right]$, and unstable otherwise. In the general case a further critical value $T_{\mathrm{min}}\left(\vartheta_c^0, \Xi\right)$ of τ^* exists such that the equilibrium configuration $p_2(\tau^*)$ is stable when $\tau^* \in \left[T_{\mathrm{min}}\left(\vartheta_c^0, \Xi\right), T_{\mathrm{Max}}\left(\vartheta_c^0, \Xi\right)\right]$, and unstable elsewhere.

Appendix E. The critical value $\bar{m}$ for curved substrates

The function $T^m_{\mathrm{Max}}\left(\vartheta_c^0, \Xi\right)$ is defined in the interval $\left(\bar{\vartheta_c}^1(\Xi, m), \bar{\vartheta_c}^2(\Xi, m)\right)$ whose length depends on the value of ϑ_c^2 introduced in appendix C. In fact, if we fix Ξ and m while varying ϑ_c^0, the length of the m-stable interval attains its maximum when $\vartheta_c^0 = \vartheta_c^{ms}(\Xi, m)$. On moving the value of ϑ_c^0 away from ϑ_c^{ms}, the point ϑ_c^2 moves towards $\bar{\vartheta_c}^{(1)}$ and the m-stable

interval shrinks. Since ϑ_c^0 is a continuous parameter, it is possible to find two values of ϑ_c^0, say $\bar{\vartheta}_c{}^1(\Xi, m) < \vartheta_c^{ms}$ and $\bar{\vartheta}_c{}^2(\Xi, m) > \vartheta_c^{ms}$ for which $\vartheta_c^2 \equiv \bar{\vartheta}_c{}^{(1)}$ and so the m-stable interval reduces to a single point ϑ_c^2 where the functions $\Theta\left(\vartheta_c \middle| \vartheta_c^0, \Xi\right)$ and $S^m\left(\vartheta_c \middle| \vartheta_c^0, \Xi\right)$ have the same slope. If $\vartheta_c^0 < \bar{\vartheta}_c{}^1(\Xi, m)$ or $\vartheta_c^0 > \bar{\vartheta}_c{}^2(\Xi, m)$ the point ϑ_c^2 does not exist and hence the function $T^m_{\mathrm{Max}}\left(\vartheta_c^0, \Xi\right)$ cannot be defined (see figure 15). As a second step we fix Ξ and ϑ_c^0 to show that the function $T^m_{\mathrm{Max}}\left(\vartheta_c^0, \Xi\right)$ cannot be defined if m is sufficiently large. Now, ϑ_c^2 exists when m is sufficiently small. On increasing m, since $S^m\left(\vartheta_c \middle| \vartheta_c^0, \Xi\right)$ tends to the x-axis, ϑ_c^2 moves on the right towards the right-end point of the m-stable interval. Thus, for a sufficiently large value $m_{\vartheta_c^0}$ of m, the unique intersection between $\Theta\left(\vartheta_c \middle| \vartheta_c^0, \Xi\right)$ and $S^m\left(\vartheta_c \middle| \vartheta_c^0, \Xi\right)$ is $\bar{\vartheta}_c{}^{(1)}$—the unique root of $\Theta\left(\vartheta_c \middle| \vartheta_c^0, \Xi\right)$—and ϑ_c^2 disappears (figure 16). If m is further increased, the function $T^m_{\mathrm{Max}}\left(\vartheta_c^0, \Xi\right)$ cannot be defined. The critical value $\bar{m}$ introduced in section 4 is then

$$\bar{m} = \max_{\vartheta_c^0 \in [0,\pi]} \left\{ m_{\vartheta_c^0} \right\}.$$

References

[1] Aveyard R, Binks B P and Clint J H 2003 Emulsions stabilised solely by colloidal particles *Adv. Colloid Interface Sci.* **100–102** 503–46

[2] Binks B P and Lumsdon S O 2000 Catastrophic phase inversion of water-in-oil emulsions stabilized by hydrophobic silica *Langmuir* **16** 2539–47

[3] Levine S and Bowen B D 1991 Capillary interaction of spherical particles adsorbed on the surface of an oil/water droplet stabilized by the particles: part I *Colloid Surf.* **59** 377–96

[4] Levine S and Bowen B D 1992 Capillary interaction of spherical particles adsorbed on the surface of an oil/water droplet stabilized by the particles: part II *Colloid Surf.* **65** 273–86

[5] Aveyard R, Clint J H and Horozov T S 2003 Aspects of the stabilisation of emulsions by solid particles: effects of line tension and monolayer curvature energy *Phys. Chem. Chem. Phys.* **5** 2398–409

[6] Steigmann D J and Li D 1995 Energy-minimizing states of capillary systems with bulk, surface, and line phases *IMA J. Appl. Math.* **55** 1–17

[7] Solomentsev Y and White L R 1999 Microscopic drop profiles and the origins of line tension *J. Colloid Interface Sci.* **218** 122–36

[8] Rowlinson J S and Widom B 2002 *Molecular Theory of Capillarity* (New York: Dover)

[9] Boruvka L and Neumann A W 1977 Generalization of the classical theory of capillarity *J. Chem. Phys.* **66** 5464–76

[10] Bieker T and Dietrich S 1998 Wetting of curved substrates *Physica* A **252** 85–137

[11] Brinkmann M, Kierfeld J and Lipowsky R 2005 Stability of liquid channels or filaments in the presence of line tension *J. Phys.: Condens. Matter* **17** 2349–64

[12] Guzzardi L, Rosso R and Virga E G 2006 Residual stability of sessile droplets with negative line tension *Phys. Rev.* E **73** 021602

[13] Aveyard R and Clint J H 1996 Particle wettability and line tension *J. Chem. Soc. Faraday Trans.* **92** 85–9

[14] Tolman R 1949 The effect of droplet size on surface tension *J. Chem. Phys.* **17** 333–7

[15] Rosso R and Verani M Curvature corrections for wetting functionals, in preparation

[16] Rosso R and Virga E G 2004 Local stability for a general wetting functional *J. Phys. A: Math. Gen.* **37** 3989–4015

Rosso R and Virga E G 2004 Corrigendum *J. Phys. A: Math. Gen.* **37** 8751

[17] Yeh E K, Newman J and Radke C J 1999 Equilibrium configurations of liquid droplets on solid surfaces under the influence of thin-film forces: I. Thermodynamics *Colloid Surf.* A **156** 137–44

[18] Yeh E K, Newman J and Radke C J 1999 Equilibrium configurations of liquid droplets on solid surfaces under the influence of thin-film forces: II. Shape calculations *Colloid Surf.* A **156** 525–46

[19] Wang J Y, Betelu S and Law M 2001 Line tension approaching a first-order wetting transition: experimental results from contact angle measurements *Phys. Rev.* E **63** 031601

[20] do Carmo M P 1976 *Differential Geometry of Curves and Surfaces* (Englewood Cliffs, NJ: Prentice-Hall)

[21] Lebedev N N 1972 *Special Functions and Their Applications* (New York: Dover)

[22] Widom B 1995 Line tension and the shape of a sessile drop *J. Phys. Chem.* **99** 2803–6

[23] Guzzardi L and Rosso R 2006 Exotic effects of line tension on curved substrates, in preparation

[24] Guzzardi L 2005 Modelling wetting with line tension *PhD Thesis* University of Florence
[25] Dong L and Johnson D T 2005 Adsorption of acicular particles at liquid-fluid interfaces and the influence of line tension *Langmuir* **21** 3838–49
[26] Gautschi W 1997 *Numerical Analysis: An introduction* (Basel: Birkhauser)
[27] Petkovic M S, Stefanovic L V and Marjanovic Z M 1992 A family of simultaneous zero finding methods *Int. J. Comput. Math.* **43** 111–26
[28] Petkovic M S and Marjanovic Z H 1991 A class of simultaneous methods for the zeros of analytic functions *Comput. Math. Appl.* **22** 79–87